Journal of Materials Chemistry A

ROYAL SOCIETY OF CHEMISTRY

PAPER

View Article Online
View Journal | View Issue

Cite this: J. Mater. Chem. A, 2025, 13, 18571

Toward enhanced combustion gas monitoring and capture: sulfur vacancies as vectors for selective CO and CO_2 intercalation in MoS_2†

Dominik M. Florjan, [a] Piotr Radomski [b] and Maciej J. Szary *[a]

Molecular intercalation holds significant implications for the effective utilization of two-dimensional (2D) materials in a wide array of key applications, including gas detection and catalysis. However, its full potential remains underexplored. Using density functional theory (DFT) simulations, this study examines the intercalation of carbon monoxide (CO) and carbon dioxide (CO_2) into molybdenum disulfide (MoS_2) and the impact of sulfur vacancies on the process. Our findings reveal that CO intercalation is universally unfavorable in pristine MoS_2, while CO_2 intercalation is marginally favorable only at high molecular coverages. Sulfur vacancies, however, serve as selective vectors, facilitating CO intercalation by incorporating CO molecules into the vacancy sites and enabling catalytic CO-to-CO_2 conversion without significantly affecting CO_2 intercalation. The extent of enhancement in CO intercalation correlates with the vacancy concentration, highlighting the potential of defect engineering in MoS_2 for a number of potential applications. This mechanism offers a promising approach for CO detection in CO + CO_2 gas mixtures, which combines an intrinsic feedback loop for elevated gas capture in MoS_2 under conditions of incomplete combustion. Additionally, sulfur vacancies support CO oxidation back to CO_2, suggesting new opportunities for the CO_2 reduction reaction (CRR) and advancing the design of multifunctional catalytic systems based on 2D materials.

Received 3rd February 2025
Accepted 29th April 2025

DOI: 10.1039/d5ta00889a

rsc.li/materials-a

1. Introduction

In the dynamic landscape of materials science and chemistry, two-dimensional materials (2DMs) have emerged as a promising frontier with transformative potential in various applications, including energy harvesting, advanced electronics, optics, sensors, and catalysis.[1–3] As research continues to unfold, the intricate physicochemistry of 2DMs promises to unlock further opportunities, solidifying their pivotal role in future technologies.[4–7] Among 2DMs, graphene and transition-metal dichalcogenides (TMDs) stand out as the most popular and extensively investigated due to their unique properties, tunability, and well-established fabrication methods.[8–12] The latter ensures sheet quality, thus providing more repeatable and controllable behavior compared to other 2DMs, which positions them as the most viable for technological and commercial applications.[13,14] These original materials hold significant potential for advancements in cutting-edge technologies, resulting in a deep interest in processes on their surfaces and interfaces.[15–20] Despite years of notable interest, the mechanisms describing such interplay are not fully understood. Consequently, the full exploitation of observed properties is currently not possible, leading to less confident adoption of the materials as part of innovative solutions. One noteworthy example is intercalation. Being prime representatives of the van der Waals (vdW) crystal family, multilayered graphene and TMDs consist of stacked, weakly interacting sheets, naturally making them excellent for intercalating various species. This interaction mode has been relatively broadly studied for graphene,[21–25] but far less frequently addressed in the context of TMDs other than in a few selected cases.[26]

One of the most obvious motivations for studying intercalation is energy storage applications since the phenomenon forms the basic principle behind the use of 2DMs in batteries and supercapacitors. Accordingly, much of the research on this subject has been done for alkali metals.[27–32] However, with this very focus, a broader technological context of intercalation receives little consideration in comparison, especially as it pertains to unintentional molecular contaminants. Thus, intercalation is generally not considered for most electronic and optical components comprising 2DMs, even when exposed to air, as in the case of sensors.[33–37] It is also consistently not explored in terms of many technological processes, including those based on atomic layer deposition (ALD), even when small molecular reagents such as water are used.[38] The interplay

[a]Institute of Physics, Poznan University of Technology, ul. Piotrowo 3, Poznan, 61-138, Poland. E-mail: maciej.szary@put.poznan.pl

[b]Institute of Materials Research and Quantum Engineering, Poznan University of Technology, ul. Piotrowo 3, Poznan, 61-138, Poland

† Electronic supplementary information (ESI) available. See DOI: https://doi.org/10.1039/d5ta00889a

between intercalation and catalysis also remains mostly unexplored.[39,40] To illustrate this substantial knowledge gap, it was only in 2023 that NO_2 intercalation was first considered for a molybdenum ditelluride ($MoTe_2$) bilayer,[41] despite NO_2 being the main target analyte for TMD-based sensors,[35–37] with no other studies addressing similar issues.

As we argued above, intercalation in the context of TMDs and graphene is generally not well explored outside of alkali intercalants. In principle, other species should also be able to intercalate, provided that the sum of exothermic intercalant–sheet interactions exceeds the endothermic interlayer expansion energy they induce. As such, small-molecule intercalation may also be favorable, although without sufficient insight into the physicochemical properties and well-examined likelihoods of occurrence, its recognition, mitigation, or use remains challenging. One important example calling for more investigations concerns cases of contaminant intercalation along with the desired intercalant, possibly limiting the overall performance of devices such as batteries. If intercalation for such species is energetically favorable and these are present during the fabrication or in the operating atmosphere, the process will typically occur. This could result in less consistent and stable properties and parameters of fabricated structures, the reproducibility of which is of great importance in electronics and optics. Naturally, there would be some competition among species to intercalate, making it essential to identify which contaminants might have a harmful impact. It would also seem that one can prevent the introduction of unwanted intercalants by providing appropriate production conditions and then, depending on the intended use, by isolating the device from the environment with a passivation layer using techniques such as ALD.[38,42,43] Nonetheless, given the gaps in current knowledge, such shielding processes themselves could potentially facilitate undesired intercalation, as they often involve high temperatures and small molecular reagents. An example that supports such claims can be the impact of the ALD on the charge carrier concentration in graphene.[44,45] Given the origin of the original carrier concentrations from spontaneous polarization at the interface,[46] observed changes can potentially arise from the intercalation of water. Despite this, the possibility remains unexplored, posing a challenge in understanding the consistent properties of 2DMs.

So far, it may seem that intercalation is primarily an undesirable effect, but this need not always be the case. It could have interesting implications in the context of catalysis, as the process would introduce more surface area for the reagents. More than that, the compression imposed on the intercalants by the sheets has the potential to facilitate novel reactions that are not observed upon absorption.[41] For similar reasons, informed utilization of intercalation may also benefit the development of novel gas sensors. To this date, 2DMs have been vastly investigated in this role, especially in the case of NO_2.[47–51] Unique intrinsic properties and a high surface-to-volume ratio led to severe advantages of such sensors, *i.e.* ppb detection limits, excellent selectivity, and fast responses. Nevertheless, the vast majority of the research concerns only adsorption-related effects. Since chemiresistors' response is represented by the change in the electrical conductivity of the sensing layer resulting from the charge transfers between the layer and the adsorbates,[52] intercalation should intrinsically improve sensitivity. This is because it allows more surface area of the sensing material to interact with the analyte. Consequently, this could be the reason why the NO_2 response for a 5-layer molybdenum disulfide (MoS_2) was found to be several times greater than that for a bilayer MoS_2, while the effect was notably smaller for ammonia (NH_3).[53] Furthermore, this same principle could underlie the improved response and recovery characteristics of interlayer-expanded VS_2 at room temperature.[54]

The selectivity and enhanced sensitivity promised by the utilization of intercalation can be potentially further exploited by defect engineering. The impact of vacancy doping on the reactivity of 2DMs is clear, as it introduces new active sites that enhance molecule–surface interactions.[55] Here, a definite advantage of TMDs over graphene arises: in the latter material, even a one-atom vacancy results in the formation of a through-hole, causing adverse changes in the mechanical and electrical properties.[56] Having three layers of atoms, TMDs are naturally more resistant to similar consequences, allowing for much more aggressive surface modification. With the increase in this reactivity, also come selectivity benefits, resulting from the geometrical constraints of the vacancies. Predictions of the behavior of different intercalants would allow for such constraints to be used to restrain the enhanced intercalation mechanism to the species of a given shape and size. Described improvements relative to pristine TMDs appear to hold great potential for designing selective and sensitive, cutting-edge sensors. However, it should be noted that intercalation would prolong the recovery time. There is common confusion regarding this parameter for many 2DM-based sensors, where weak physisorption on the surface is expected, but recovery at room temperature takes minutes to hours.[36,53] Intercalation could be one of the contributing factors; thus, the insights would help develop strategies to mitigate this effect and shorten the time.

Intercalation has broad implications and can affect the use of TMDs in most of their applications. As such, it needs to be well understood and accounted for before their intrinsic properties can be fully exploited and they can be confidently adopted in technological innovations. We want to emphasize here again the role of these materials in the context of gas sensors, the development of which is more and more necessary every day due to global air pollution problems. Carbon dioxide (CO_2) and carbon monoxide (CO), being the adverse products of fossil fuel combustion, represent prime examples of molecules that should be strictly controlled. While the first one carries long-term damage as a widespread greenhouse gas, the latter endangers the population more directly, leading to an increased risk of ischaemic heart disease, stroke, asthma, and cancer.[57,58] Despite the remarkable success of TMDs in NO_2 detection, the CO_2 and CO ones leave much to be desired. The fundamental reason is their lack of a significant dipole moment, compared to *e.g.* NO_2, making them not as susceptible to interaction through vdW forces, the primary mode of adsorption on pristine TMDs' surfaces.[50,59,60] Theoretically, the little detector response can be

enhanced by employing an intercalation-based approach, increasing the surface area exposed to interaction and, thus, sensitivity. Another approach is to vacancy dope the layer. Such treatment would create new active adsorption sites, potentially unlocking new modes of interaction. The question remains whether both CO and CO_2 will react to vacancies in the same manner – if smaller CO would benefit more due to easier access to the site, the effect may be used for selective detection. In this way, one could control the completeness of combustion processes or monitor the CO level in the CO_2-rich atmospheres of today's agglomerations. In this regard, we present the first-principle study of CO_2 and CO intercalation between two monolayers of MoS_2, pristine or with single-atom sulfur vacancies. This TMD was specifically chosen due to its widespread use in NO_2 sensors[35,61–64] and well-established fabrication methods,[65–68] allowing for controlled defect introduction. Moreover, MoS_2 is known to catalyze the reduction of carbon dioxide.[69–72] The reaction, especially hydrogenation to methanol, can be further optimized by utilizing vacancy-rich layers;[73,74] nonetheless, the studies mainly focus on exposed-surface physics, disregarding the impact of intercalation. Our investigations on MoS_2 have not been limited only to describing the effects due to the presence of vacancies but also take into account different molecular coverages. The latter parameter was proven to influence the response of $MoTe_2$;[41] hence, it is expected to be of significance in the case of akin MoS_2. The presented theoretical insights provide a sound basis for a highly sensitive MoS_2-based CO sensor, an incomplete combustion detector, or a selective catalyst.

2. Computational details

In silico modeling presented in the study utilized the DFT framework based on plane waves, and ultrasoft pseudopotentials (USPPs), as implemented in the QUANTUM ESPRESSO suite.[75–77] The employed pseudopotentials included scalar-relativistic and nonlinear core corrections. The plane-wave cutoff energies were set at 50 Ry for the wave function and at 500 Ry for the electron density. The integration of the Brillouin zone was done with a Monkhorst–Pack grid[78] of $4 \times 4 \times 1$. Several trials were conducted to assess optimal cutoff energies and *k*-point grids until higher values showed minimal impact on the modeled intercalation process. During structure optimization, all atoms' positions were adjusted until the force and the total energy reached convergence criteria of less than 10^{-3} Ry au^{-1} and 10^{-4} Ry, respectively. For this purpose, the Broyden–Fletcher–Goldfarb–Shanno (BFGS)[79–82] quasi-Newton algorithm was used. The partial charges were established with Löwdin[83] population analysis, considering only the influence of the valence electrons and omitting the core ones.

Given the substantial influence of electronic states near the Fermi level on molecule-sheet interactions, we initially evaluated several exchange–correlation (XC) functionals, including the generalized gradient approximation (GGA)-based Perdew–Burke–Ernzerhof (PBE) functional,[84,85] the hybrid Heyd–Scuseria–Ernzerhof (HSE) functional, and the Hubbard *U* correction. However, these more computationally intensive approaches did not yield significant improvements in the accuracy of the calculated adsorption properties to warrant their continued use. This observation aligns with a substantial body of literature that effectively employs PBE-based methodologies in similar systems.[86–89] On the other hand, because the basal plane of pristine TMDs is chemically inert, interactions with CO_2 and CO molecules are predominantly governed by van der Waals (vdW) forces.[50,90] Consequently, selecting an appropriate vdW correction is critical. In this context, dispersion correction schemes such as Grimme's D3 method[91,92] are widely used in combination with the PBE functional to capture these weak interactions accurately.[60,93–96]

Given the focus on intercalation in multilayer TMDs, it is essential that the computational approach accurately captures both in-plane and out-of-plane structural parameters. To evaluate the reliability of the chosen PBE + D3 framework, we compared the calculated lattice constants with those obtained using several non-local correlation functionals: vdW-DF-OBK8,[97] vdW-DF-OB86,[98] and vdW-DF2-B86R,[99] alongside available experimental data. The results show that the PBE + D3 approach exhibits strong agreement with experimental values (see Fig. 1), performing comparably to—or in some cases better than—the tested non-local functionals. These findings validate the accuracy and robustness of the adopted computational methodology.

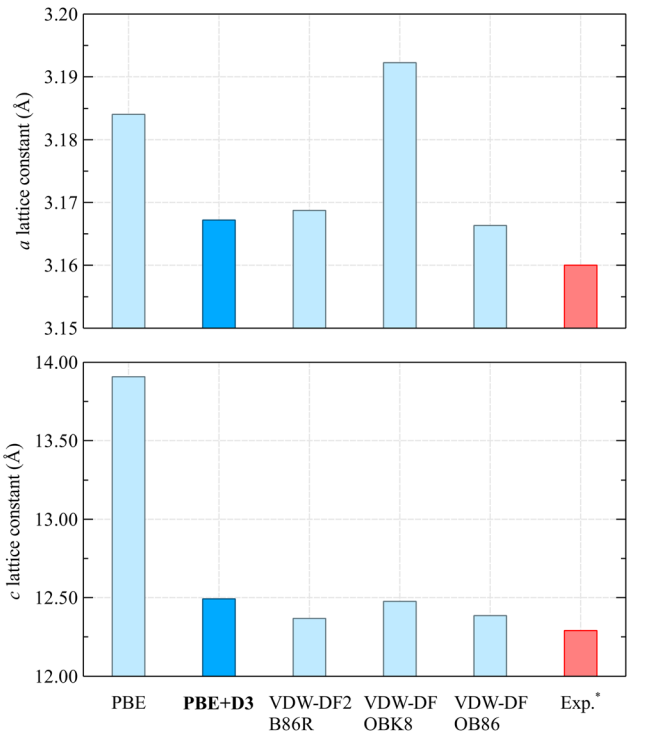

Fig. 1 Comparison of *a* lattice constants of 2H-MoS_2 obtained for the PBE functional without and with the D3 correction, as well as for non-local correlation functionals: vdW-DF2-B86R,[99] vdW-DF-OBK8,[97] and vdW-DF-OB86.[98] The *experimental values of $a = 3.16$ Å and $c = 12.29$ Å for bulk MoS_2 were taken from studies of Bronsema *et al.*[100] and Joensen *et al.*[101]

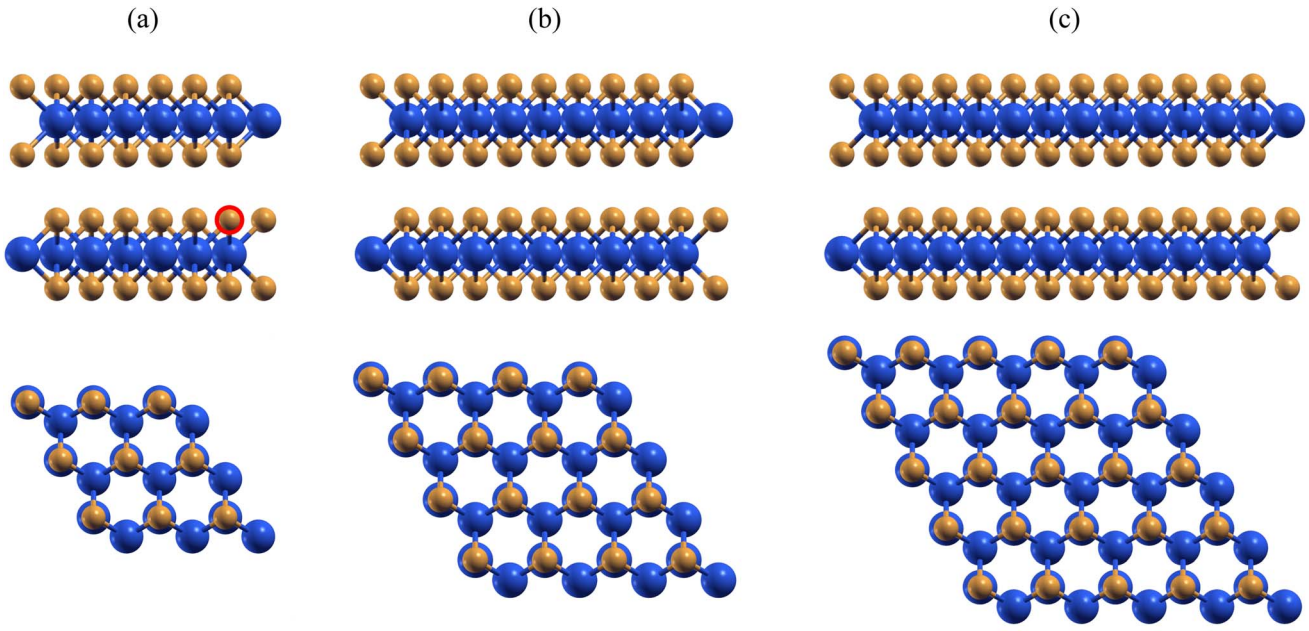

Fig. 2 Supercells of pristine MoS_2: (a) 3 × 3, (b) 4 × 4, and (c) 5 × 5. Sulfur and molybdenum atoms are colored yellow and blue, respectively. Vacancy-doped systems were obtained by removing a single S atom from the lower sheet, as shown by the red circle in panel (a).

To asses vibrational contributions of CO and CO_2 we have employed the density functional perturbation theory (DFPT) approach as implemented using the PHONON.X code of QUANTUM ESPRESSO. The free molecules were relaxed and perturbed in a cubic cell with the same volume as that of the hexagonal cell employed for MoS_2 calculations, allowing a similar density of plane-wave basis and proper isolation to be achieved. All of the parameters were the same as those for the rest of this work, except for the three-body term inclusion in D3 correction due to software limitations.

When calculating the properties of two-dimensional systems under periodic boundary conditions, images created in the *z*-axis may artificially affect the interactions. To mitigate this effect, cell height was set to 32 Å. Atomic structures included in Fig. 2–6 were rendered using the XcrySDen program.[102] Graphs presented in Fig. 3–6 and 7 were made with the Veusz package.[103]

3. Results and discussion

3.1. Intercalation modeling approach

To explore the behavior of intercalated CO_2 and CO, three kinds of bilayer MoS_2 supercells were prepared: 3 × 3, 4 × 4, and 5 × 5. These structures are shown in Fig. 2. The dimensions of a system in question will be given in parentheses after referencing the number of molecules (mol) contained within. Employing more than a single supercell allows for the investigation of a broad range of molecular coverages from 0.462 to 7.704 molecules nm^{-2} for CO_2, *i.e.* from 1 × CO_2 (5 × 5) to 6 × CO_2 (3 × 3), and from 0.462 to 10.272 molecules nm^{-2} for CO, *i.e.* from 1 × CO (5 × 5) to 8 × CO (3 × 3 MoS_2). Such an approach seems crucial since the amount of intercalant may significantly affect the process, as it was previously shown for NO_2 between $MoTe_2$.[41] During the preliminary studies, we explored several initial placements of the molecules to identify the most favorable configurations. Some positions were selected based on structural symmetry, such as the one located in the hollow site above the center of a triangle formed by the nearest-neighboring sulfur atoms. Other configurations were obtained using *ab initio* molecular dynamics. From these simulations, we selected a few local-minima configurations, which were subsequently optimized. The intercalation energies of all cases were then examined to identify the most favorable configurations. For higher coverage scenarios, where multiple molecules occupy each unit cell, the intercalants were distributed evenly across the interface, adopting the previously identified lowest-energy configurations as the initial orientation, which were then optimized.

The essential parameter allowing for quantitative analysis of intercalants behavior is intercalation energy E_{int} defined as

$$E_{int} = E_{endo} + E_{exo} \equiv E(\text{mol} + 2\text{L}) - E(\text{mol}) - E(2\text{L}) \quad (1)$$

This quantity is the sum of energies resulting from the endothermic interlayer expansion (E_{endo}) and exothermic molecule–sheet interaction (E_{exo}) and can be further written as the difference between the energy of the whole intercalation system (E(mol + 2L) and the sum of free molecules E(mol) and pristine sheet (E(2L)) energies. Individually the exothermic and endothermic energies are expressed as:

$$E_{exo} = E(\text{mol} + 2\text{L}) - E(\text{mol}) - E(\text{IE} - 2\text{L}) \quad (2)$$

$$E_{endo} = E(\text{IE} - 2\text{L}) - E(2\text{L}). \quad (3)$$

From these equations, it becomes evident that the strength of intercalation is the result of the combat between the favorable molecule-layer interaction and the work devoted to the geometric deformation of the material. A negative E_{int} indicates a generally favorable intercalation process, whereas a positive E_{int} suggests that the process is unfavorable.

Previous studies have demonstrated that TMDs hold great potential for the detection of small molecules such as NO or NO_2.[36,37,47,49,50,64] However, the fully saturated metal-chalcogen bonds leave the surfaces chemically inert, significantly reducing the list of potential analytes. Their activity can be significantly enhanced through techniques such as doping the layers with p-block elements[94,95] or introducing vacancy sites.[55] In this work, we utilize the latter approach, simulated by the removal of a single sulfur atom from the sheet surface, as demonstrated using the red circle in Fig. 2. Note that due to the different sizes of the studied layers, the respective concentrations of vacancies are not identical, though the mode of interactions associated with their occurrence is strongly local and presents itself completely only with 2 or more molecules per vacancy. For this reason, the vacant MoS_2 systems describing the lowest coverages, *i.e.* 5×5, 4×4, and 3×3 supercells with one intercalant, seem reasonable to be directly compared.

The fundamental factor affecting the TMD-based sensors' response is the change in the charge carrier concentration. Hence, the parameter of substantial importance is the charge transfer δQ, calculated according to the formula:

$$\delta Q = Q(\text{intercalated}) - Q(\text{free}). \quad (4)$$

being the difference between the total charge of intercalated species and their free (in vacuum) counterparts. Additionally, upon intercalation, the weakly bonded layers of TMDs tend to separate significantly, increasing the interlayer distance and creating a larger gap that accommodates molecules. Such distancing happens at the expense of molecular-sheet bonding energy, resulting in the lowering of mutual interaction strength. In this study, we define the total distance between the layers d using

$$d = z(\text{avg. S upper}) - z(\text{avg. S lower}), \quad (5)$$

where z(avg. S upper) is the averaged z coordinate of the uppermost S atoms in the lower layer and z(avg. Te lower) is the averaged z coordinate of the lowermost S atoms in the upper layer.

3.2. Intercalation of CO and CO_2 between pristine MoS_2

Intercalation energy is a key parameter for assessing the capacity of an intercalant to penetrate and stabilize within layered structures. For CO_2 intercalation into MoS_2 layers, the intercalation energy values are shown in Fig. 3a as purple circles, alongside the constituent endothermic and exothermic components, represented by green diamonds and red squares, respectively. Detailed numerical values are provided in Table 1. The analysis indicates that CO_2 intercalation is largely unfavorable over most of the investigated coverage range. The highest intercalation energy of 1.43 eV nm^{-2} is observed at the lowest coverage of 0.462 molecules nm^{-2}, underscoring a strongly unfavorable process. As molecular coverage increases, E_{int} decreases, eventually crossing into the negative (favorable) range at a coverage of 5.136 molecules nm^{-2}, where it reaches -0.049 eV nm^{-2}. Beyond this point, E_{int} continues to decline gradually, achieving -0.262 eV nm^{-2} at the highest coverage investigated, 7.704 molecules nm^{-2}.

The trend is primarily driven by the reduction in E_{exo}, which reflects the strength of interactions between the intercalants and the layers. At low coverages, E_{exo} remains slightly below zero, indicating weak interactions between individual molecules and the upper and lower monolayers. This is illustrated in Fig. 3d, where CO_2 molecules lie flat, maintaining a substantial distance from the MoS_2 sheets. As molecular coverage increases, E_{exo} decreases, indicating enhanced intercalation strength per unit area due to a greater number of molecules interacting with the monolayers rather than an increase in interaction strength per molecule. Individual CO_2 molecules interact minimally with MoS_2, as evidenced by the small charge transfer, which does not exceed $-0.05\ e$ (see Fig. 3b). From 1.284 molecules nm^{-2} to 6.420 molecules nm^{-2}, the total charge transfer (δQ) increases linearly with the number of CO_2 molecules, while the average per-molecule charge transfer remains nearly constant. At higher coverage values, the growth of total δQ diminishes due to spatial constraints forcing the molecules into a vertical orientation, as shown in Fig. 3f. This reorientation results in greater layer expansion, which reduces electron transfer efficiency and affects the interlayer distance. These structural changes directly influence the intercalation energy.

The structural impact on the MoS_2 monolayers is further illustrated by the total interlayer distance d, as shown in Fig. 3c. This distance expands progressively with increasing intercalant density, with a prominent jump at 7.704 molecules nm^{-2}, caused by the reorientation of CO_2 molecules (refer to Fig. 3d–f). The energy required for such expansion is quantified using E_{endo}, which increases sharply at low coverage due to the significant interlayer separation necessary to accommodate the initial intercalants. Subsequently, E_{endo} increases more gradually with higher coverage and larger interlayer distances. Even at low intercalant densities, E_{endo} surpasses E_{exo}, thereby hindering favorable intercalation until a coverage of 5.136 molecules nm^{-2}. Importantly, E_{endo} does not exceed the energy difference between a bilayer and two separate monolayers, $2 \times E$(monolayer) $- E(2 \times$ monolayer). This finding indicates that while interlayer interactions are significantly weakened, the monolayers are not fully decoupled by the intercalants. Overall, the interaction between layers and intercalants is predominantly van der Waals in nature. This is corroborated by the lack of geometric distortion in CO_2 molecules (see top views in Fig. 3d–f), minimal charge transfers, and high intercalation energies, which exclude the possibility of chemical bonding. The inert nature of pristine MoS_2 surfaces is consistent with these observations. Furthermore, the absence of a CO_2 dipole moment, due to its symmetry, limits the efficiency of physisorption through vdW-based mechanisms.

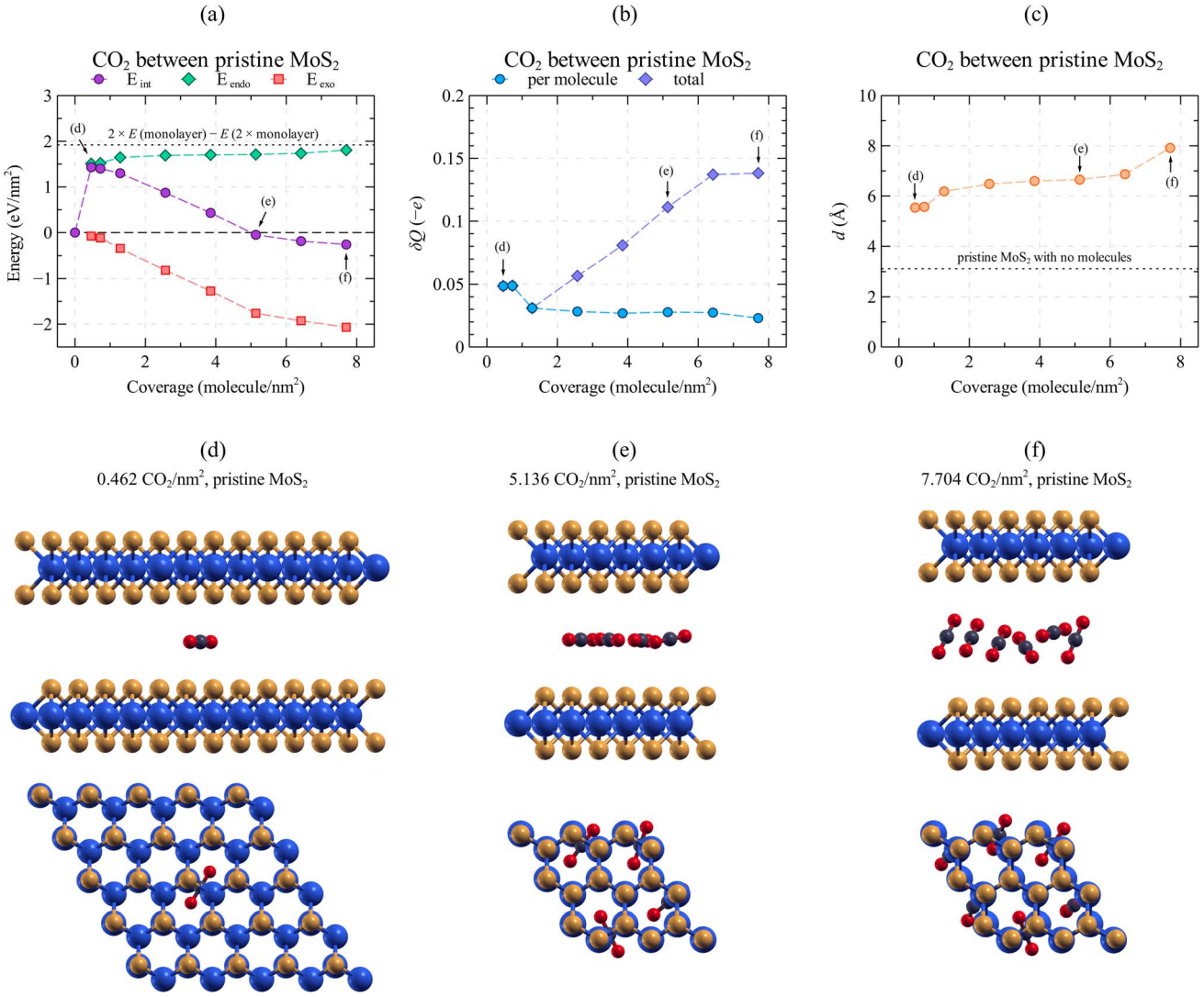

Fig. 3 Graphs characterizing CO_2 intercalated between two pristine MoS_2 monolayers: (a) intercalation energy with endothermic and exothermic contributions, (b) total charge transfer and charge transfer averaged per molecule, and (c) distance between relaxed layers, all plotted as a function of sheet coverage. Subfigures (d)–(f) contain selected relaxed configurations corresponding to the points marked with arrows.

Given the vdW nature of interactions between layers and intercalants, one might expect CO to exhibit intercalation behavior similar to that of CO_2. However, this is not the case. Fig. 4a–c illustrate the intercalation energies, charge transfers, and interlayer distances for CO, with numerical data summarized in Table 1. This consistent representation highlights key differences that become immediately apparent. The most notable distinction lies in the E_{int}-coverage relationship, depicted in Fig. 4a. At low coverage (0.462 molecules nm^{-2}), CO exhibits a maximum intercalation energy of 1.507 eV nm^{-2}, comparable to CO_2. However, as coverage increases, E_{int} decreases, following a trend similar to CO_2. Unlike CO_2, though, the intercalation energy for CO remains positive across the entire coverage range, signifying consistently unfavorable intercalation. The lowest E_{int} value, 0.238 eV nm^{-2}, occurs at 7.704 molecules nm^{-2}, after which the curve begins to rise. Additionally, E_{int} values for CO are consistently higher than those for CO_2 across all coverage levels, underscoring CO's weaker affinity for MoS_2 layers.

The exothermic energy follows a similar trend, suggesting that the energy behavior at higher coverages is more attributable to the intrinsic nature of CO-sheet interactions than to effects related to disparity in MoS_2 expansion. Charge transfers, shown in Fig. 4b, are quantitatively comparable to those of CO_2, remaining below −0.05 *e*. This indicates that higher molecular coverage does not enhance induced dipole moments in the intercalated molecules and, by extension, does not enhance vdW-driven molecule–sheet interactions. The steady, nearly linear increase in total δQ and the consistent per-molecule δQ across the coverage range reveal that these quantities are independent of the number of intercalants. Consequently, adding more CO molecules does not lead to any qualitative changes or favorable intercalation behavior.

Table 1 Intercalation parameters for CO_2 and CO between pristine MoS_2. The quantities are defined using eqn (1), (3), (2), (4) and (5). Here, the symbol δQ represents the total charge transfer from the sheet to all atoms of the given system molecules

System	Coverage (molecules nm^{-2})	E_{int} (eV nm^{-2})	E_{endo} (eV nm^{-2})	E_{exo} (eV nm^{-2})	δQ ($-e$)	d (Å)
1 × CO_2 5 × 5	0.462	1.430	1.507	−0.077	0.049	5.54
1 × CO_2 4 × 4	0.722	1.400	1.519	−0.119	0.049	5.57
1 × CO_2 3 × 3	1.284	1.299	1.646	−0.347	0.031	6.19
2 × CO_2 3 × 3	2.568	0.872	1.690	−0.818	0.057	6.48
3 × CO_2 3 × 3	3.852	0.431	1.703	−1.273	0.081	6.60
4 × CO_2 3 × 3	5.136	−0.049	1.711	−1.760	0.111	6.65
5 × CO_2 3 × 3	6.420	−0.188	1.736	−1.924	0.137	6.87
6 × CO_2 3 × 3	7.704	−0.262	1.806	−2.067	0.138	7.91
1 × CO 5 × 5	0.462	1.529	1.613	−0.084	0.044	6.01
1 × CO 4 × 4	0.722	1.450	1.523	−0.073	0.066	5.60
1 × CO 3 × 3	1.284	1.436	1.661	−0.225	0.034	6.27
2 × CO 3 × 3	2.568	1.162	1.699	−0.538	0.062	6.55
3 × CO 3 × 3	3.852	0.845	1.708	−0.863	0.077	6.63
4 × CO 3 × 3	5.136	0.566	1.720	−1.154	0.100	6.74
5 × CO 3 × 3	6.420	0.301	1.731	−1.431	0.145	6.85
6 × CO 3 × 3	7.704	0.238	1.740	−1.503	0.174	6.95
7 × CO 3 × 3	8.988	0.396	1.759	−1.363	0.224	7.17
8 × CO 3 × 3	10.272	0.717	1.784	−1.067	0.262	7.52

The interlayer distance d, plotted in Fig. 4c, varies from approximately 6 to nearly 8 Å, reflecting a gradual and smooth expansion of the sheets as intercalants position themselves vertically. This behavior is visualized in Fig. 4d–f, which show MoS_2 configurations at coverages of 0.462, 7.704, and 10.272 molecules nm^{-2}, respectively. For any given number of CO molecules, d is slightly larger than that in the corresponding CO_2 system. The associated E_{endo}, which accounts for the energy required for this layer expansion, combined with the weak molecule-layer interactions, makes pristine MoS_2 suboptimal for CO intercalation.

The differences between CO and CO_2 intercalation originate from the nature of molecule-sheet interactions. Beyond 7.704 molecules nm^{-2}, the total exothermic energy for CO increases rather than decreases. One might attribute this to potential repulsion between neighboring intercalants. However, if such repulsion were significant, it would manifest more prominently for CO_2, a larger molecule, and likely lead to the formation of a second molecular layer at the interface, which is not observed. Instead, this behavior is likely a consequence of molecular orientation. At higher coverages, CO molecules reorient from a flat to a vertical alignment, a configuration that is less energetically favorable for CO compared to CO_2 (Table 2).

3.3. Unlocking the CO and CO_2 intercalation potential *via* single-atom vacancy doping

While our findings for pristine monolayers indicate that the intercalation of CO and CO_2 is generally unfavorable, this analysis does not fully capture the intercalation behavior in MoS_2. Even high-quality monolayers inevitably possess defects, among which sulfur vacancies are particularly significant. These vacancies can alter the reactivity of basal planes and create sites conducive to the incorporation of intercalants. Thus, such defects could, in principle, act as facilitators—or vectors—for intercalation, enabling a process that would otherwise be energetically unfavorable. As a result, the intercalation capacity of real-world MoS_2 structures may surpass the predictions of pristine models, potentially increasing the prevalence of unintentional intercalation depending on the quality of the sheets. Moreover, if sulfur vacancies significantly enhance intercalation favorability, they could be intentionally engineered to optimize MoS_2 sheets for specific applications, presenting new opportunities for material design and functionalization. To investigate this, we examine the intercalation of CO and CO_2 using a defective MoS_2 model, where single sulfur vacancies are introduced at the interface. Specifically, one sulfur atom per supercell is removed from the upper sulfur layer of the lower MoS_2 monolayer (see Fig. 2a). To ensure the reliability of our results, the model structures used in this study incorporate experimentally realistic defect concentrations. These vacancy levels can be practically achieved in MoS_2 through various established methods, including salt-assisted chemical vapor deposition (CVD).[104]

The effects of vacancies on the intercalation of CO_2 are shown in Fig. 5, where the parameters are presented in the same format as that for pristine MoS_2 to allow direct comparison. The vertical and horizontal scales remain consistent across cases. The results indicate that the E_{int} curve for defective MoS_2 is qualitatively and quantitatively similar to that of the pristine sheet. Across the range of 0.722 molecules nm^{-2} to 5.136 molecules nm^{-2}, E_{int} values differ by no more than 0.12 eV nm^{-2}. Thus, as in pristine MoS_2, intercalation energy in defective MoS_2 is highest at low molecular coverage and decreases gradually, becoming negative near 5.2 molecules nm^{-2} before continuing to decline. Relative to pristine MoS_2, intercalation of CO_2 becomes energetically favorable at slightly higher coverage in the sulfur-deficient system. However, this

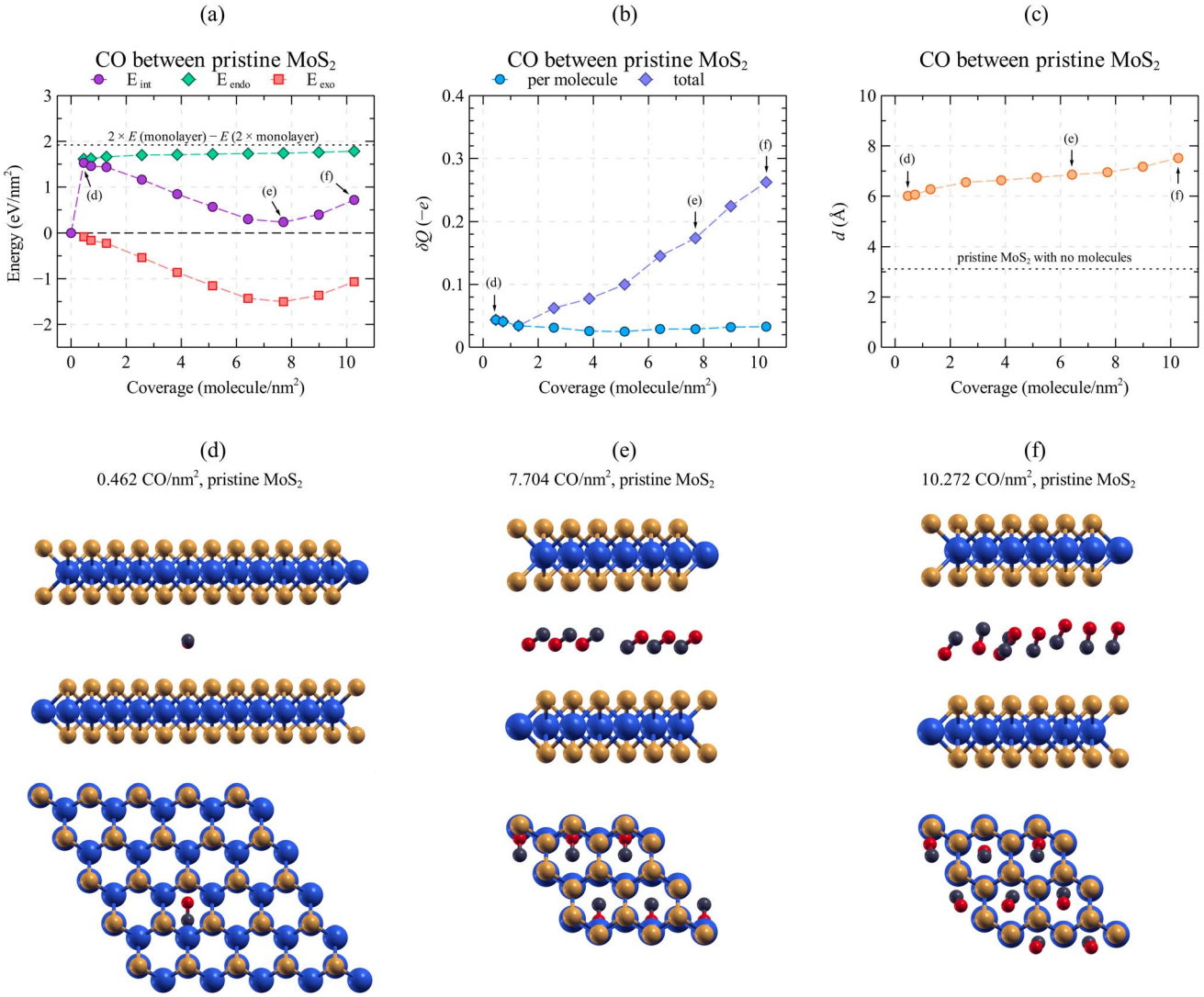

Fig. 4 Graphs characterizing CO intercalated between two pristine MoS_2 monolayers: (a) intercalation energy with endothermic and exothermic contributions, (b) total charge transfer and charge transfer averaged per molecule, and (c) distance between relaxed layers, all plotted as a function of sheet coverage. Subfigures (d)–(f) contain selected relaxed configurations corresponding to the points marked with arrows.

Table 2 Intercalation parameters for CO_2 and CO between vacancy-doped MoS_2. The quantities are defined using eqn (1), (3), (2), (4) and (5). Here, the symbol δQ represents the total charge transfer from the sheet to all atoms of the given system molecules

System	Coverage (molecules nm^{-2})	E_{int} (eV nm^{-2})	E_{endo} (eV nm^{-2})	E_{exo} (eV nm^{-2})	δQ ($-e$)	d (Å)
1 × CO_2 4 × 4	0.722	1.406	1.538	−0.132	0.045	5.65
1 × CO_2 3 × 3	1.284	1.237	1.593	−0.357	0.030	6.05
2 × CO_2 3 × 3	2.568	0.895	1.648	−0.753	0.044	6.42
3 × CO_2 3 × 3	3.852	0.465	1.662	−1.197	0.077	6.53
4 × CO_2 3 × 3	5.136	0.004	1.671	−1.667	0.101	6.61
5 × CO_2 3 × 3	6.420	−0.300	1.688	−1.988	0.153	6.76
1 × CO 4 × 4	0.722	−0.620	0.074	−0.701	0.486	3.18
1 × CO 3 × 3	1.284	−1.159	0.207	−1.393	0.469	3.25
2 × CO 3 × 3	2.568	−1.048	1.481	−2.730	0.584	5.35
3 × CO 3 × 3	3.852	−1.244	1.641	−3.078	0.608	6.02
4 × CO 3 × 3	5.136	−1.499	1.699	−3.392	0.623	6.39
5 × CO 3 × 3	6.420	−1.860	1.706	−3.755	0.630	6.45
6 × CO 3 × 3	7.704	−2.031	1.738	−3.959	0.669	6.73
7 × CO 3 × 3	8.988	−2.139	1.760	−4.090	0.687	6.97
8 × CO 3 × 3	10.272	−2.359	1.783	−4.333	0.726	7.27

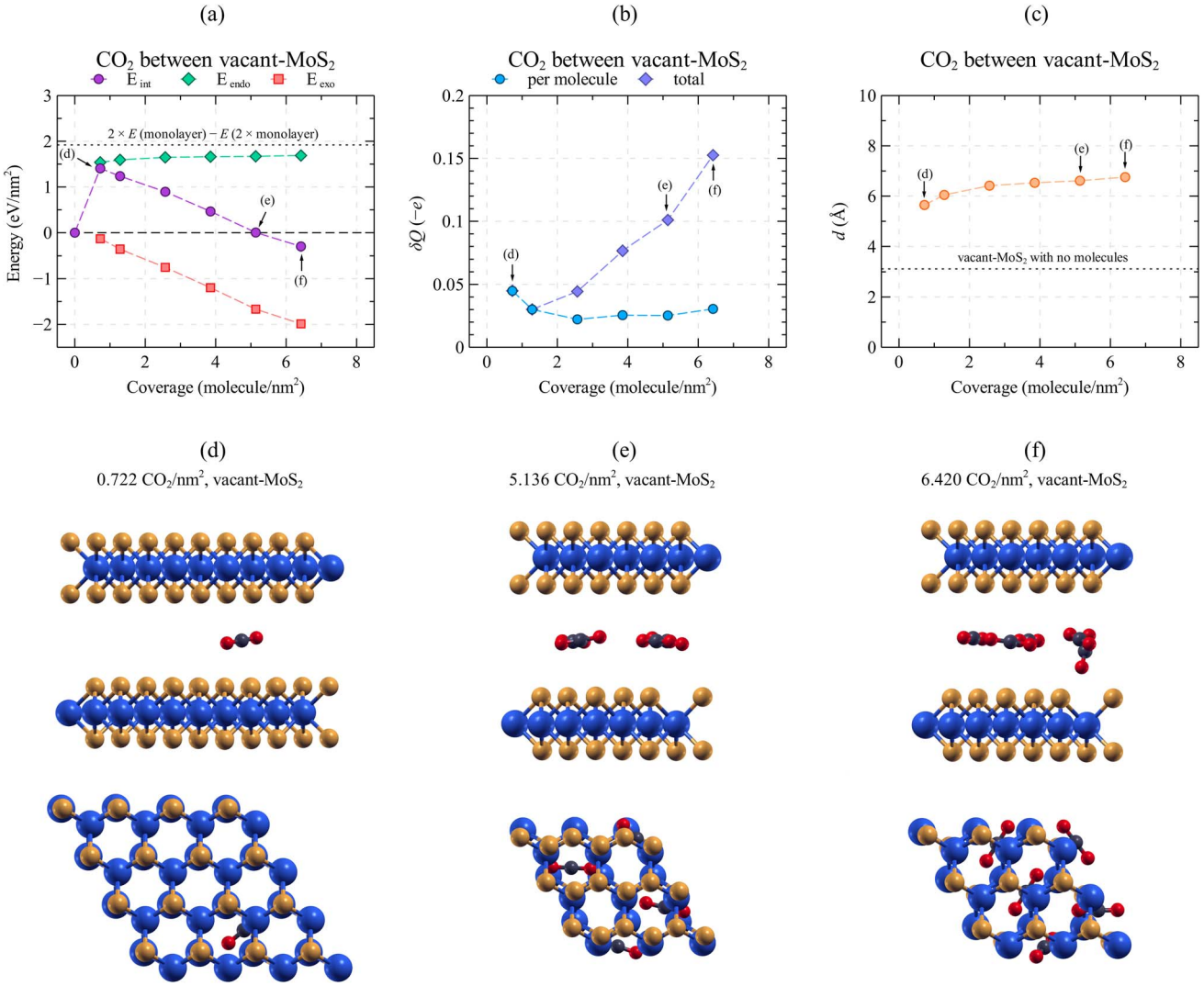

Fig. 5 Graphs characterizing CO_2 intercalated between one pristine and one vacancy-doped MoS_2 monolayer: (a) intercalation energy with endothermic and exothermic contributions, (b) total charge transfer and charge transfer averaged per molecule, and (c) distance between relaxed layers, all plotted as a function of sheet coverage. Subfigures (d)–(f) contain selected relaxed configurations corresponding to the points marked with arrows.

difference is minimal, suggesting that sulfur vacancies have a negligible impact on the energetics of the intercalation process.

Yet, despite these similarities, some structural differences arise due to the presence of defects. At 6.420 molecules nm^{-2}, one CO_2 molecule reorients vertically and shifts toward the vacancy site, as illustrated in Fig. 5f. This reorientation induces a relatively sharp increase of -0.052 e in the total charge transfer between 5.136 and 6.420 molecules nm^{-2} (see Fig. 5b). However, even with this adjustment, the interaction remains within the weak physisorption regime. At significant coverage, such as 6.420 molecules nm^{-2}, no CO_2 molecule forms a chemical bond with the vacancy site, leaving the overall intercalation parameters largely unaffected by the defect. Additionally, the removal of sulfur slightly reduces the interlayer expansion d (Fig. 5c), which modestly diminishes the E_{endo} contribution. However, this effect is minor. Hence, the E_{exo} continues to decrease linearly with the addition of molecules, while E_{endo} increases sharply at low coverages and then increases only modestly with higher coverage, mirroring the behavior observed for pristine MoS_2.

The minimal influence of vacancies on CO_2 intercalation is corroborated by Fig. 5d–f, where all CO_2 molecules remain undeformed and maintain their original distance from the monolayers, with the exception of the vertically oriented molecule in Fig. 5f. The limited impact of vacancies may be attributed to the size of the CO_2 molecule, which imposes stricter geometric constraints on bonding interactions. As a result, CO_2 cannot incorporate into the vacancies and benefit from the exposure of Mo atoms at these sites. The intercalation behavior of CO_2 in defective MoS_2, therefore, is largely similar to that in pristine sheets, showing negligible impact from the introduction of sulfur vacancies.

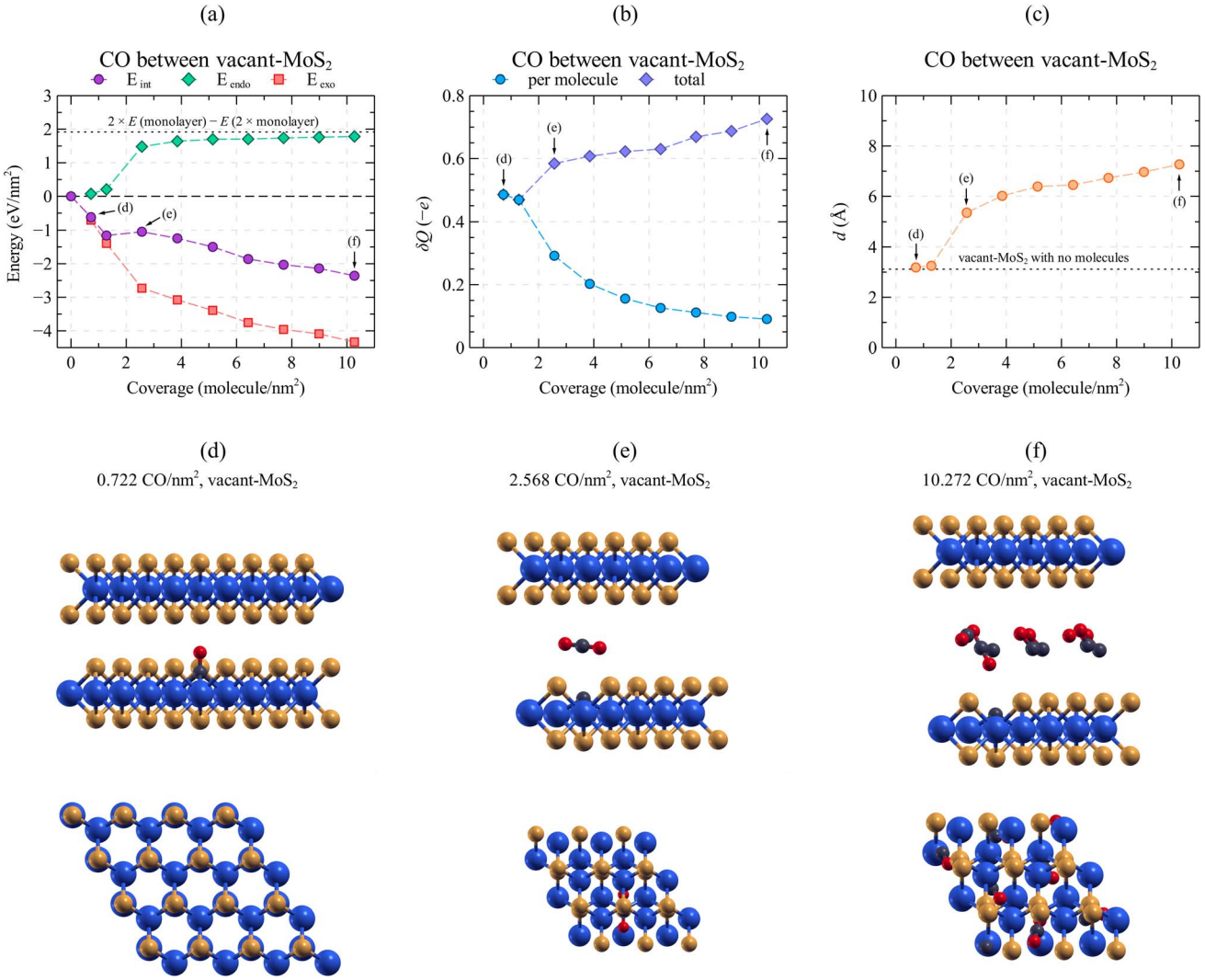

Fig. 6 Graphs characterizing CO intercalated between one pristine and one vacancy-doped MoS_2 monolayer: (a) intercalation energy with endothermic and exothermic contributions, (b) total charge transfer and charge transfer averaged per molecule, and (c) distance between relaxed layers, all plotted as a function of sheet coverage. Subfigures (d)–(f) contain selected relaxed configurations corresponding to the points marked with arrows.

In contrast, the intercalation behavior changes significantly when CO is introduced. Intercalation of CO in vacancy-doped MoS_2 is energetically favorable across the entire analyzed coverage range. The E_{int} trend is presented in Fig. 6a, with adjusted vertical scales for clarity. At 0.722 molecules nm^{-2}, the intercalation energy is -0.620 eV nm^{-2}, much lower than any value observed in previous cases, suggesting the emergence of a new mode of interaction. Indeed, CO settles directly into the vacancy, as shown in Fig. 6d. The bonding here is clearly chemical, localized, and significantly stronger than the vdW-based adsorption described earlier. High charge transfer ($\delta Q = -0.486\ e$, Fig. 6b) further confirms the chemical nature of the interaction. Additionally, upon adsorption, the C–O bond length increases to 1.21 Å compared to the original 1.13 Å of free CO, indicating partial activation of the molecule within the sulfur vacancy site of MoS_2. The interlayer distance d (Fig. 6c) is barely larger than that of intercalant-free MoS_2, as CO occupies the vacancy, minimizing the need for layer expansion. Consequently, E_{endo} is minimal, and the dominant energy contribution comes from the favorable E_{exo} due to strong binding.

At 1.284 molecules nm^{-2}, each vacancy hosts one CO molecule, resulting in interactions similar to those at its lower levels. However, at higher coverages (2.568 molecules nm^{-2} and above), where the number of CO intercalants exceeds the number of vacancies, a chemical reaction occurs: $2 \times CO \rightarrow CO_2 + C$. The resultant carbon atom bonds with the exposed Mo atoms, while CO_2 remains suspended between the layers (Fig. 6e). This reaction causes a significant increase in total charge transfer (by 0.115 e) between 1.284 molecules nm^{-2} and 2.568 molecules nm^{-2}, most of which arises from the carbon covalently bonding to the MoS_2 sheet.

Although this specific pathway has not been previously reported for MoS_2, similar vacancy-mediated oxidation processes—such as $2CO + O_2 \rightarrow 2CO_2$—have been observed,[105]

further supporting the catalytic potential of sulfur-deficient MoS_2 systems. Hence, to assess the thermodynamic feasibility of CO oxidation *via* intercalation, we considered both the zero-point energy (ZPE) and vibrational entropy S_{vib} contributions to the reaction $2CO \rightarrow CO_2 + C$. Based on the vibrational frequencies, the zero-point energy can be calculated as:

$$\mathrm{ZPE} = \sum_i \frac{1}{2} h\nu_i, \tag{6}$$

while the vibrational entropy is evaluated as[106]

$$S_{vib} = k_B \sum_i \left[\frac{h\nu_i}{k_B T} \left(e^{\frac{h\nu_i}{k_B T}} - 1 \right)^{-1} - \ln\left(1 - e^{\frac{h\nu_i}{k_B T}} \right) \right], \tag{7}$$

where k_B and h are the Boltzmann and Planck constants, T is the temperature, and ν_i is the frequency of a given vibration.

The results reveal that, at room temperature, the combined contribution of zero-point energy and vibrational entropy to the reaction amounts to a minor correction of approximately 5 meV. Given that the corresponding electronic energy change is approximately −1 eV, the reaction remains thermodynamically favorable.

It is also important to note that the carbon-doped site is expected to remain catalytically active after the reaction, owing to the distinct valence configuration of carbon compared to sulfur. This residual reactivity may promote further catalytic processes, such as the CO_2 reduction reaction (CRR), akin to those occurring at the edges of MoS_2.[69,70,107]

This chemical interaction underscores CO's sensitivity to single-atom defects. Not only does the presence of vacancies make CO intercalation immediately favorable, but it also initiates a new interaction regime capable of breaking the C–O bond. However, the oxidation product (CO_2) and the filled vacancy (now hosting a carbon atom) force the layers to expand significantly (Fig. 6c). The associated E_{endo} increase of over 1.4 eV nm^{-2} surpasses the E_{exo} gain of approximately 1.3 eV nm^{-2}, making intercalation at 2.568 molecules nm^{-2} ($E_{int} = -1.048$ eV nm^{-2}) slightly less favorable than that at 1.284 molecules nm^{-2} ($E_{int} = -1.159$ eV nm^{-2}).

However, as CO coverage increases, the cumulative molecule-sheet interaction strength grows: E_{exo} steadily decreases, reaching −4.333 eV nm^{-2} at 10.272 molecules nm^{-2}. In contrast, the increase in the cost of interlayer expansion is much more modest, resulting in overall more favorable intercalation energies. This is accompanied by an increase in total charge transfer and interlayer distance. However, the average per-molecule δQ decreases, as the vacancy's effect is localized. Once the active site is occupied by the carbon atom, subsequent CO molecules cannot directly benefit from the vacancy. This is confirmed in Fig. 6f, where additional CO molecules remain suspended between the MoS_2 layers. The lone CO_2 molecule near the vacancy adopts a near-vertical orientation, likely due to spatial constraints rather than attraction to the defect. Thus, the behavior of CO intercalation in defective MoS_2 is dominated by strong local interactions at vacancy sites, followed by weaker interactions akin to those in pristine systems. With asymptotic E_{endo} behavior, E_{int} is primarily driven by E_{exo}, achieving −2.359 eV nm^{-2} at 10.272 molecules nm^{-2}.

Taken together, the introduction of vacancies dramatically alters MoS_2's response to CO intercalants. Unlike CO_2, the interaction mechanism shifts from weak vdW forces to strong chemisorption at vacancy sites. This highly localized effect depends on the vacancy-to-CO ratio. While further CO coverage after vacancy saturation still leads to favorable intercalation, the greatest energetic payoff occurs when the number of CO molecules matches the number of vacancies, minimizing energy losses due to interlayer expansion. Consequently, the higher the density of sulfur vacancies in MoS_2, the greater the propensity for CO intercalation.

3.4. Evaluating the selectivity and strength of vacancy-induced enhancement

The results demonstrate that sulfur vacancies in MoS_2 can have a significant qualitative impact on intercalation, substantially enhancing its favorability for CO while exerting minimal influence on CO_2. To quantify the effect of vacancies and illustrate this selectivity, Fig. 7 presents the changes in E_{int}, δQ, and d between pristine and vacancy-doped MoS_2 for both intercalants. These differences are defined as follows:

$$\Delta E_{int} = E_{int}(\text{vacant}) - E_{int}(\text{pristine}) \tag{8}$$

$$\Delta \delta Q = \delta Q(\text{vacant}) - \delta Q(\text{pristine}) \tag{9}$$

$$\Delta d = d(\text{vacant}) - d(\text{pristine}) \tag{10}$$

It is evident from Fig. 7a–c that CO_2 remains largely unaffected by the presence of vacancies, as indicated by the near-zero differences in E_{int}, δQ, and d. The flat trend lines across molecular coverages indicate no significant modulation of these parameters. On one hand, this finding excludes vacancy doping as a viable strategy for enhancing the intercalation of CO_2 in MoS_2, limiting its utility for MoS_2 sheet engineering or for employing vacancy-induced sensitivity enhancement mechanisms. On the other hand, this suggests that unintentional intercalation of CO_2 is generally unlikely and the structural quality of the layer is less critical in mitigating such occurrences. Furthermore, this behavior minimizes the potential for competing effects arising from widespread CO_2 following vacancy-induced optimization to other intercalants.

In contrast, CO intercalation is significantly enhanced in defective MoS_2. Fig. 7a shows a substantial reduction in intercalation energy, with values decreasing by approximately −2 eV nm^{-2} at a minimum and exceeding −3 eV nm^{-2} at 10.272 molecules nm^{-2}. This highlights the prevailing effect of vacancies, regardless of whether their per-area concentration equals or is less than that of the molecules. Substantial changes are also observed in charge transfer, particularly at low coverages, with a gradual decrease as coverage increases. Thus, sulfur vacancies not only serve as effective vectors for enhancing CO intercalation in MoS_2, but their impact scales with higher vacancy concentrations, amplifying the sheet's response. The geometric impact on MoS_2 is equally pronounced. The vacancy-

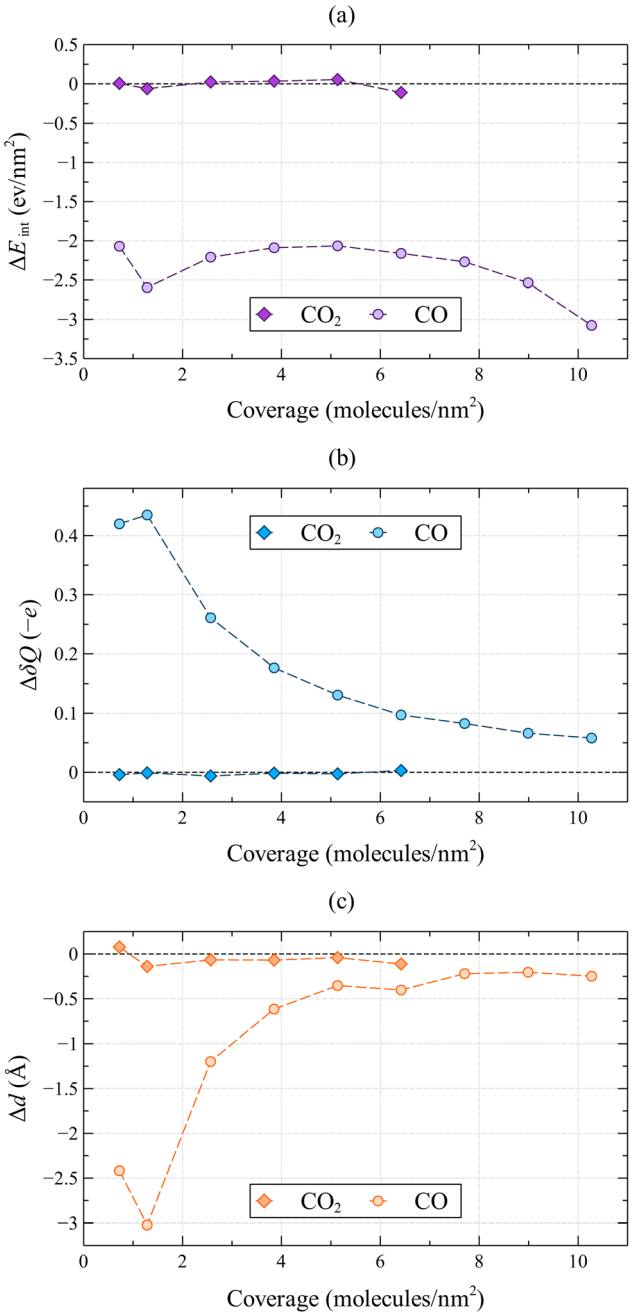

Fig. 7 Differences in intercalation parameters induced by the vacancy introduction for CO_2 and CO: (a) intercalation energy, (b) charge transfer, and (c) distance between relaxed layers. Definitions are given using eqn (8)–(10).

filling by intercalated CO or by a carbon atom released during oxidation allows the layers to maintain a significantly reduced interlayer distance compared to pristine MoS_2, reaching as low as 3 Å at 1.284 molecules nm^{-2}. All CO-related curves in Fig. 7a–c exhibit local extrema at this coverage, indicating that this concentration is optimal for leveraging the benefits of vacancies.

Furthermore, considering the behavior of gas mixtures adds an additional layer of complexity. A primary factor opposing favorable CO_2 intercalation is the endothermic layer expansion, which requires over 1.5 eV nm^{-2}. However, the highly exothermic oxidation of CO counteracts this energy expense, leaving the MoS_2 structure significantly expanded. In such a system, additional CO_2 molecules can intercalate more easily since the layers would not need to separate further to accommodate them. This reduces the E_{endo} contribution and mitigates the reduction in E_{int}. Consequently, even a small amount of CO mixed with CO_2 could influence the intercalation process of the latter, presenting new opportunities for CO detection mechanisms or, conversely, increasing the risk of facilitating access for unwanted intercalants in technological applications.

3.5. Potential of vacancy engineered MoS_2 for intercalation-based applications

The promotion of intercalation driven by sulfur vacancies and its high selectivity position vacancy-doped MoS_2 as a promising material for various technological applications. One clear example is its potential use in CO chemisorption-based gas sensors. To date, MoS_2 and other TMDs have had limited success in detecting CO and similar analytes with weak dipole moments due to low adsorption energies and insufficient charge transfer, which result in poor sensitivity and selectivity.[51,60,108] Vacancy doping addresses these limitations by improving both the sensitivity and selectivity of CO detection in CO + CO_2 mixtures.

While the present study focuses on CO and CO_2 intercalation, the findings may have broader implications for gas selectivity. Intercalation is inherently a competitive process, governed by the balance between the endothermic energy cost of interlayer expansion and the exothermic energy gain from molecule–sheet interactions. Among commonly encountered gases in ambient environments—such as H_2O, O_2, CO_2, and CO—differences in molecular size are relatively minor. Therefore, the key differentiating factor is the adsorption energy of each species on the TMD surface. Prior studies on MoS_2 have shown that the adsorption energies of H_2O and O_2 are approximately 75% of that of CO,[51,109] indicating that CO is more strongly bound. This suggests that the enhanced CO sensitivity and selectivity observed in our work should remain robust under typical environmental conditions. Additionally, it may offer further benefits for long-term environmental stability, as the lower intercalation competitiveness of H_2O and O_2 is expected to intrinsically limit their ability to interfere with the intercalation process or passivate vacancy sites. Such behavior would be generally consistent with the well-documented hydrophobic nature of MoS_2 basal planes.[110]

Under clean combustion conditions, CO_2 alone struggles to intercalate effectively. However, even a small amount of CO in the mixture can enhance the intercalation process. The reaction 2 × CO → CO_2 + C facilitates interlayer expansion in MoS_2, which subsequently makes CO_2 intercalation easier. This cascade effect enhances the cumulative response of the layer by modulating the carrier concentration through charge-transfer mechanisms in intercalated multilayer systems (see Fig. 8), thereby improving its sensitivity to CO in CO + CO_2 mixtures.

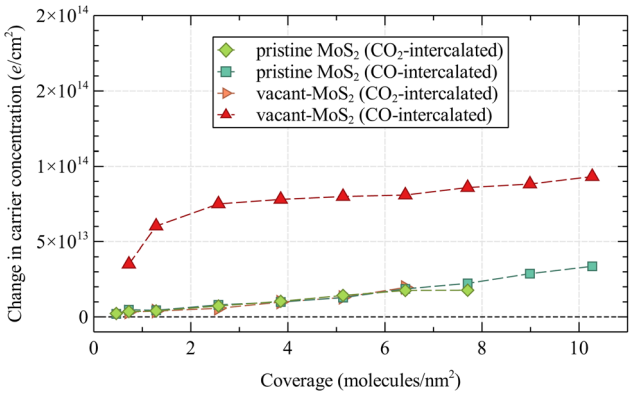

Fig. 8 Change in the charge carrier concentration upon CO_2 or CO intercalation for pristine and vacant-MoS_2 as a function of molecular coverage. Positive values correspond to p-type doping of the sheets.

Our model predicts carrier concentrations in the range of 10^{12} to 10^{13} $e$cm^{-2} representing substantial levels of p-type doping arising solely from the intercalation process—comparable to doping levels commonly reported for MoS_2.[111] Moreover, this mechanism may function as a positive feedback loop, promoting increased gas uptake in MoS_2 under conditions such as those present during incomplete combustion.

Such a monitoring system could play a critical role in regulating fossil fuel combustion atmospheres and managing carbon dioxide reduction rates. By strategically incorporating sulfur vacancies or dopants such as niobium, the rates and products of these reactions can be precisely controlled.[70,73,74] While some methods target the synthesis of methanol or methane, CO production is also frequently observed.[72] Notably, vacancy engineering has been shown to facilitate the conversion of CO into methanol.[73,74] Our analysis reveals that in the absence of sufficient oxygen or hydrogen, vacancies can alternatively support CO oxidation back to CO_2, creating renewed opportunities for reduction processes.

Integrating intercalation into this context shifts the focus of MoS_2 functionalization efforts from edge-specific tailoring to bulk engineering. This approach allows for the functionalization of layers during crystal growth and the exposed surfaces of multilayered MoS_2. With sufficient sulfur removal, intercalation between vacancy-doped MoS_2 layers could also serve as an efficient CO capture mechanism, particularly at coverages below 2.568 molecules nm^{-2}. The saturation of such a system could be readily identified through a sharp change in the MoS_2 carrier concentration (see Fig. 8), corresponding to the rapid growth in total charge transfer.

For a more quantitative evaluation, CHNO elemental analysis can be employed to assess molecular coverage accurately. This method has been successfully used to determine the intercalation levels of NH_4^+ in MoS_2.[112] Another viable method of monitoring CO or CO_2 intercalation involves detecting swelling in the MoS_2 structure. The shift in interaction mode from CO adsorption in vacancies ($\leq$1.284 molecules nm^{-2}) to CO oxidation ($\geq$2.568 molecules nm^{-2}) results in a layer expansion exceeding 64%. This substantial structural change would manifest as detectable lattice constant variations in a multilayered crystal. Intercalation in bulk MoS_2 crystals could thus be monitored using techniques such as interferometry, Raman spectroscopy, or other industrially viable methods, as charge and strain in 2D materials are known to produce measurable intercalation effects.[113–116] Additionally, the piezoelectric properties of MoS_2-based structures, which have already been demonstrated,[117–119] could provide another avenue for exploiting these changes.

The interplay of intercalation and sulfur vacancy engineering unlocks a wide array of potential device enhancements and introduces new modes of interaction, paving the way for innovative applications. The insights provided by this analysis not only support the development of next-generation intercalation and defect-engineered TMD devices but also offer explanations for the previously unexplained differences between multilayered and monolayered MoS_2 systems. Furthermore, our insights into intercalation favorability suggest that structural variations across different TMD materials—such as differences in van der Waals gap sizes and lattice constants—could give rise to distinct intercalation behaviors. This adds an additional dimension for tuning the performance of TMD-based systems and may also enable improved detection selectivity when different TMDs are employed in tandem.

4. Conclusions

This paper investigates *in silico* studies of CO and CO_2 intercalation between layers of MoS_2, analyzing the effects of single-atom sulfur vacancies and molecular coverage on structural expansion, intercalation energy, and charge transfer. The results demonstrate that both pristine and vacancy-doped sheets are highly sensitive to the intercalant concentration, with distinct behaviors observed for CO and CO_2. For CO_2, increasing molecular coverage consistently reduces intercalation energy in both pristine and defective sheets, yielding negative values at coverages above 5.136 molecules nm^{-2}. Interestingly, sulfur vacancies have a minimal impact on this process, suggesting that defects play a negligible role in CO_2 intercalation. In contrast, CO exhibits markedly different behavior. In pristine MoS_2, CO intercalation is universally endothermic and energetically unfavorable across all studied coverages. However, the presence of sulfur vacancies transforms the process into an exothermic one for all investigated coverages. This enhancement stems from two distinct mechanisms:

(1) CO molecules incorporate into sulfur vacancies, forming chemical bonds between the carbon atom of CO and exposed molybdenum atoms.

(2) Remaining CO molecules interact with these incorporated molecules, triggering an oxidation reaction ($2 \times CO \rightarrow CO_2 + C$). This reaction converts two CO molecules into one CO_2 molecule and a free carbon atom, with the remaining carbon incorporated within the sulfur vacancy.

As a result, the extent of enhancement in CO intercalation is strongly correlated with the vacancy concentration. This finding highlights the potential of defect engineering in MoS_2, where

higher defect densities enable increased intercalation and facilitate substantial charge transfer. The dominant contribution to total charge transfer arises from the formation of C–Mo bonds, which are inherently limited by the density of sulfur vacancies. Notably, these mechanisms are absent for CO_2, explaining why its intercalation parameters remain similar in pristine and defective sheets. However, varying vacancy sizes may present new opportunities for tuning sheet properties.

This study establishes a foundational framework for designing gas sensors based on vacancy-doped multilayer MoS_2. Such sensors should exhibit heightened sensitivity to CO, significantly outperforming pristine sheets, with notable selectivity as reflected in the distinct responses to CO and CO_2. Furthermore, the intercalation-driven approach offers a promising pathway for CO detection in CO + CO_2 gas mixtures, leveraging an intrinsic feedback loop that enhances gas capture under incomplete combustion conditions. Finally, the findings also offer insights into potential faults in TMD-based devices. Intercalated CO, prevalent in some operational environments, could unintentionally affect device performance. While pristine MoS_2 is resistant to such contamination, achieving completely vacancy-free TMD layers remains a significant challenge even with advanced synthesis techniques. Additionally, the vacancy-driven CO oxidation reaction sheds new light on the catalytic potential of TMDs, emphasizing the need for further exploration of their applications in confined catalysis.

Data availability

The data supporting this article have been included as part of the ESI.

Conflicts of interest

There are no conflicts to declare.

Acknowledgements

This work was funded by the Ministry of Education and Science in Poland within the project “Perły Nauki” under Grant No. PN/01/0058/2022. Calculations reported in this work were performed at the Interdisciplinary Center for Mathematical and Computational Modeling (ICM) of the University of Warsaw under Grant No. G96-1893.

References

1 A. Gupta, T. Sakthivel and S. Seal, Recent development in 2D materials beyond graphene, *Prog. Mater. Sci.*, 2015, **73**, 44–126, DOI: **10.1016/j.pmatsci.2015.02.002**.

2 D. Akinwande, C. J. Brennan, J. S. Bunch, P. Egberts, J. R. Felts, H. Gao, R. Huang, J.-S. Kim, T. Li, Y. Li, K. M. Liechti, N. Lu, H. S. Park, E. J. Reed, P. Wang, B. I. Yakobson, T. Zhang, Y.-W. Zhang, Y. Zhou and Y. Zhu, A review on mechanics and mechanical properties of 2D materials—graphene and beyond, *Extreme Mech. Lett.*, 2017, **13**, 42–77, DOI: **10.1016/j.eml.2017.01.008**.

3 C. Anichini, W. Czepa, D. Pakulski, A. Aliprandi, A. Ciesielski and P. Samorì, Chemical sensing with 2D materials, *Chem. Soc. Rev.*, 2018, **47**, 4860–4908, DOI: **10.1039/C8CS00417J**.

4 A. J. Mannix, B. Kiraly, M. C. Hersam and N. P. Guisinger, Synthesis and chemistry of elemental 2D materials, *Nat. Rev. Chem*, 2017, **1**(2), 0014, DOI: **10.1038/s41570-016-0014**.

5 G. Liu, C. Zhen, Y. Kang, L. Wang and H.-M. Cheng, Unique physicochemical properties of two-dimensional light absorbers facilitating photocatalysis, *Chem. Soc. Rev.*, 2018, **47**, 6410–6444, DOI: **10.1039/C8CS00396C**.

6 F. R. Fan, R. Wang, H. Zhang and W. Wu, Emerging beyond-graphene elemental 2D materials for energy and catalysis applications, *Chem. Soc. Rev.*, 2021, **50**, 10983–11031, DOI: **10.1039/C9CS00821G**.

7 V. Shanmugam, R. A. Mensah, K. Babu, S. Gawusu, A. Chanda, Y. Tu, R. E. Neisiany, M. Försth, G. Sas and O. Das, A review of the synthesis, properties, and applications of 2D materials, *Part. Part. Syst. Charact.*, 2022, **39**(6), 2200031, DOI: **10.1002/ppsc.202200031**.

8 S. K. Tiwari, S. Sahoo, N. Wang and A. Huczko, Graphene research and their outputs: Status and prospect, *J. Sci.:Adv. Mater. Devices*, 2020, **5**(1), 10–29, DOI: **10.1016/j.jsamd.2020.01.006**.

9 W. Yu, L. Sisi, Y. Haiyan and L. Jie, Progress in the functional modification of graphene/graphene oxide: a review, *RSC Adv.*, 2020, **10**, 15328–15345, DOI: **10.1039/D0RA01068E**.

10 T. Chowdhury, E. C. Sadler and T. J. Kempa, Progress and prospects in transition-metal dichalcogenide research beyond 2D, *Chem. Rev.*, 2020, **120**(22), 12563–12591, DOI: **10.1021/acs.chemrev.0c00505**, pMID: 32960576.

11 M. Wang, H. Li, T.-J. Ko, M. S. Shawkat, E. Okogbue, C. Yoo, S. S. Han, M. A. Islam, K. H. Oh and Y. Jung, Manufacturing strategies for wafer-scale two-dimensional transition metal dichalcogenide heterolayers, *J. Mater. Res.*, 2020, **35**(11), 1350–1368, DOI: **10.1557/jmr.2020.27**.

12 F. G. Aras, A. Yilmaz, H. G. Tasdelen, A. Ozden, F. Ay, N. K. Perkgoz and A. Yeltik, A review on recent advances of chemical vapor deposition technique for monolayer transition metal dichalcogenides (MX_2: Mo, W; S, Se, Te), *Mater. Sci. Semicond. Process.*, 2022, **148**, 106829, DOI: **10.1016/j.mssp.2022.106829**.

13 M. T. uddeen Safian, K. Umar and M. N. Mohamad Ibrahim, Synthesis and scalability of graphene and its derivatives: A journey towards sustainable and commercial material, *J. Cleaner Prod.*, 2021, **318**, 128603, DOI: **10.1016/j.jclepro.2021.128603**.

14 S. A. Iyengar, S. Bhattacharyya, S. Roy, N. R. Glavin, A. K. Roy and P. M. Ajayan, A researcher’s perspective on unconventional lab-to-fab for 2D semiconductor devices, *ACS Nano*, 2023, **17**(14), 12955–12970, DOI: **10.1021/acsnano.3c01927**, pMID: 37405421.

15 C. Riedl, C. Coletti, T. Iwasaki, A. A. Zakharov and U. Starke, Quasi-free-standing epitaxial graphene on SiC obtained by hydrogen intercalation, *Phys. Rev. Lett.*, 2009, **103**, 246804, DOI: **10.1103/PhysRevLett.103.246804**.

16 T. Ciuk, S. Cakmakyapan, E. Ozbay, P. Caban, K. Grodecki, A. Krajewska, I. Pasternak, J. Szmidt and W. Strupinski, Step-edge-induced resistance anisotropy in quasi-free-standing bilayer chemical vapor deposition graphene on SiC, *J. Appl. Phys.*, 2014, **116**(12), 123708, DOI: 10.1063/1.4896581.

17 S. Si, J. Wang, J. Li, W. Li, H. Cong, J. Liu, J. Tang, C. Jiang, R. Xia and X. Xiao, Enhancing resistance to radiation hardening and radiation thermal conductivity degradation by tungsten/graphene interface engineering, *J. Nucl. Mater.*, 2020, **539**, 152348, DOI: 10.1016/j.jnucmat.2020.152348.

18 W. Peng and K. Sun, Effects of cu/graphene interface on the mechanical properties of multilayer Cu/graphene composites, *Mech. Mater.*, 2020, **141**, 103270, DOI: 10.1016/j.mechmat.2019.103270.

19 Y. Sun, Y. Wang, J. Y. C. Chen, K. Fujisawa, C. F. Holder, J. T. Miller, V. H. Crespi, M. Terrones and R. E. Schaak, Interface-mediated noble metal deposition on transition metal dichalcogenide nanostructures, *Nat. Chem.*, 2020, **12**(3), 284–293, DOI: 10.1038/s41557-020-0418-3.

20 S. Aftab, M. Z. Iqbal, M. W. Iqbal, M. Asghar and H. Ullah, Recent advances in tmd interfaces with seamless contacts, *J. Mater. Chem. C*, 2022, **10**, 14795–14811, DOI: 10.1039/D2TC02734H.

21 E. J. Olson, R. Ma, T. Sun, M. A. Ebrish, N. Haratipour, K. Min, N. R. Aluru and S. J. Koester, Capacitive Sensing of Intercalated H_2O Molecules Using Graphene, *ACS Appl. Mater. Interfaces*, 2015, **7**(46), 25804–25812, DOI: 10.1021/acsami.5b07731.

22 J. Wan, S. D. Lacey, J. Dai, W. Bao, M. S. Fuhrer and L. Hu, Tuning two-dimensional nanomaterials by intercalation: materials, properties and applications, *Chem. Soc. Rev.*, 2016, **45**(24), 6742–6765, DOI: 10.1039/C5CS00758E.

23 Y. Zhou, B. Li, L. Wang, J. Zhou, K. He, W. Li, J. Li, X. Hu, Y. Liu, L. Liao and X. Duan, Regulation of the Electronic Properties of Graphene via Organic Molecular Intercalation, *Chem. Mater.*, 2023, **35**(5), 2125–2132, DOI: 10.1021/acs.chemmater.2c03753.

24 P. Sutter, J. T. Sadowski and E. A. Sutter, Chemistry under Cover: Tuning Metal-Graphene Interaction by Reactive Intercalation, *J. Am. Chem. Soc.*, 2010, **132**(23), 8175–8179, DOI: 10.1021/ja102398n.

25 M. J. Szary, S. El-Ahmar and T. Ciuk, The impact of partial H intercalation on the quasi-free-standing properties of graphene on SiC(0001), *Appl. Surf. Sci.*, 2021, **541**, 148668, DOI: 10.1016/j.apsusc.2020.148668.

26 Q. Zhang, L. Mei, X. Cao, Y. Tang and Z. Zeng, Intercalation and exfoliation chemistries of transition metal dichalcogenides, *J. Mater. Chem. A*, 2020, **8**(31), 15417–15444, DOI: 10.1039/D0TA03727C.

27 A. Nijamudheen, D. Sarbapalli, J. Hui, J. Rodríguez-López and J. L. Mendoza-Cortes, Impact of surface modification on the lithium, sodium, and potassium intercalation efficiency and capacity of few-layer graphene electrodes, *ACS Appl. Mater. Interfaces*, 2020, **12**(17), 19393–19401, DOI: 10.1021/acsami.9b23105, pMID: 32109048.

28 B. Chen, D. Chao, E. Liu, M. Jaroniec, N. Zhao and S.-Z. Qiao, Transition metal dichalcogenides for alkali metal ion batteries: engineering strategies at the atomic level, *Energy Environ. Sci.*, 2020, **13**, 1096–1131, DOI: 10.1039/C9EE03549D.

29 W.-B. Li, S.-Y. Lin, N. T. T. Tran, M.-F. Lin and K.-I. Lin, Essential geometric and electronic properties in stage-n graphite alkali-metal-intercalation compounds, *RSC Adv.*, 2020, **10**, 23573–23581, DOI: 10.1039/D0RA00639D.

30 I. V. Chepkasov, M. Ghorbani-Asl, Z. I. Popov, J. H. Smet and A. V. Krasheninnikov, Alkali metals inside bi-layer graphene and MoS_2: Insights from first-principles calculations, *Nano Energy*, 2020, **75**, 104927, DOI: 10.1016/j.nanoen.2020.104927.

31 J. Ma, C. Yang, X. Ma, S. Liu, J. Yang, L. Xu, J. Gao, R. Quhe, X. Sun, J. Yang, F. Pan, X. Yang and J. Lu, Improvement of alkali metal ion batteries via interlayer engineering of anodes: from graphite to graphene, *Nanoscale*, 2021, **13**, 12521–12533, DOI: 10.1039/D1NR01946E.

32 I. V. Chepkasov, J. H. Smet and A. V. Krasheninnikov, Single- and multilayers of alkali metal atoms inside graphene/MoS_2 heterostructures: A systematic first-principles study, *J. Phys. Chem. C*, 2022, **126**(37), 15558–15564, DOI: 10.1021/acs.jpcc.2c03749.

33 R. Pearce, T. Iakimov, M. Andersson, L. Hultman, A. L. Spetz and R. Yakimova, Epitaxially grown graphene based gas sensors for ultra sensitive NO_2 detection, *Sens. Actuators, B*, 2011, **155**(2), 451–455, DOI: 10.1016/j.snb.2010.12.046.

34 S. Novikov, N. Lebedeva, A. Satrapinski, J. Walden, V. Davydov and A. Lebedev, Graphene based sensor for environmental monitoring of NO_2, *Sens. Actuators, B*, 2016, **236**, 1054–1060, DOI: 10.1016/j.snb.2016.05.114.

35 R. Kumar, N. Goel and M. Kumar, UV-Activated MoS_2 Based Fast and Reversible NO_2 Sensor at Room Temperature, *ACS Sens.*, 2017, **2**(11), 1744–1752, DOI: 10.1021/acssensors.7b00731.

36 E. Wu, Y. Xie, B. Yuan, H. Zhang, X. Hu, J. Liu and D. Zhang, Ultrasensitive and fully reversible NO_2 gas sensing based on p-type $MoTe_2$ under ultraviolet illumination, *ACS Sens.*, 2018, **3**(9), 1719–1726, DOI: 10.1021/acssensors.8b00461, pMID: 30105902.

37 J. Jaiswal, A. Das, V. Chetry, S. Kumar and R. Chandra, NO_2 sensors based on crystalline $MoSe_2$ porous nanowall thin films with vertically aligned molecular layers prepared by sputtering, *Sens. Actuators, B*, 2022, **359**, 131552, DOI: 10.1016/j.snb.2022.131552.

38 T. Ciuk, L. Ciura, P. Michałowski, J. Jagiełło, A. Dobrowolski, K. Piętak, D. Kalita, M. Wzorek, R. Budzich, D. Czołak and A. Kolek, Contamination-induced inhomogeneity of noise sources distribution in Al_2O_3-passivated quasi-free-standing graphene on 4H-SiC(0001), *Phys. E*, 2022, **142**, 115264, DOI: 10.1016/j.physe.2022.115264.

39 L. Lin, P. Sherrell, Y. Liu, W. Lei, S. Zhang, H. Zhang, G. G. Wallace and J. Chen, Engineered 2d transition metal dichalcogenides—a vision of viable hydrogen

evolution reaction catalysis, *Adv. Energy Mater.*, 2020, **10**(16), 1903870, DOI: 10.1002/aenm.201903870.

40 Y. Yan, W. I. Shin, H. Chen, S.-M. Lee, S. Manickam, S. Hanson, H. Zhao, E. Lester, T. Wu and C. H. Pang, A recent trend: application of graphene in catalysis, *Carbon Lett.*, 2021, **31**(2), 177–199, DOI: 10.1007/s42823-020-00200-7.

41 M. J. Szary, Computational study of the intercalation of NO_2 between bilayer $MoTe_2$, *Appl. Surf. Sci.*, 2023, **611**, 155514, DOI: 10.1016/j.apsusc.2022.155514.

42 E. Schilirò, R. L. Nigro, S. E. Panasci, S. Agnello, M. Cannas, F. M. Gelardi, F. Roccaforte and F. Giannazzo, Direct atomic layer deposition of ultrathin aluminum oxide on monolayer MoS_2 exfoliated on gold: The role of the substrate, *Adv. Mater. Interfaces*, 2021, **8**(21), 2101117, DOI: 10.1002/admi.202101117.

43 E. Schilirò, S. Panasci, A. Mio, G. Nicotra, S. Agnello, B. Pecz, G. Radnoczi, I. Deretzis, A. La Magna, F. Roccaforte, R. Lo Nigro and F. Giannazzo, Direct atomic layer deposition of ultra-thin Al_2O_3 and HfO_2 films on gold-supported monolayer MoS_2, *Appl. Surf. Sci.*, 2023, **630**, 157476, DOI: 10.1016/j.apsusc.2023.157476.

44 T. Ciuk, A. Kozlowski, P. P. Michalowski, W. Kaszub, M. Kozubal, Z. Rekuc, J. Podgorski, B. Stanczyk, K. Przyborowska, I. Jozwik, A. Kowalik and P. Kaminski, Thermally activated double-carrier transport in epitaxial graphene on vanadium-compensated 6H-SiC as revealed by hall effect measurements, *Carbon*, 2018, **139**, 776–781, DOI: 10.1016/j.carbon.2018.07.049.

45 T. Ciuk, B. Stanczyk, K. Przyborowska, D. Czolak, A. Dobrowolski, J. Jagiello, W. Kaszub, M. Kozubal, R. Kozlowski and P. Kaminski, High-temperature hall effect sensor based on epitaxial graphene on high-purity semiinsulating 4H-SiC, *IEEE Trans. Electron Devices*, 2019, **66**(7), 3134–3138, DOI: 10.1109/TED.2019.2915632.

46 J. Sławińska, H. Aramberri, M. Muñoz and J. Cerdá, Ab initio study of the relationship between spontaneous polarization and p-type doping in quasi-freestanding graphene on h-passivated sic surfaces, *Carbon*, 2015, **93**, 88–104, DOI: 10.1016/j.carbon.2015.05.025.

47 E. Wu, Y. Xie, B. Yuan, H. Zhang, X. Hu, J. Liu and D. Zhang, Ultrasensitive and Fully Reversible NO_2 Gas Sensing Based on p-Type $MoTe_2$ under Ultraviolet Illumination, *ACS Sens.*, 2018, **3**(9), 1719–1726, DOI: 10.1021/acssensors.8b00461.

48 Z. Feng, Y. Xie, J. Chen, Y. Yu, S. Zheng, R. Zhang, Q. Li, X. Chen, C. Sun, H. Zhang, W. Pang, J. Liu and D. Zhang, Highly sensitive $MoTe_2$ chemical sensor with fast recovery rate through gate biasing, *2D Materials*, 2017, **4**(2), 025018, DOI: 10.1088/2053-1583/aa57fe.

49 M. Reddeppa, B.-G. Park, G. Murali, S. H. Choi, N. D. Chinh, D. Kim, W. Yang and M.-D. Kim, NO_x gas sensors based on layer-transferred n-MoS_2/p-GaN heterojunction at room temperature: Study of UV light illuminations and humidity, *Sens. Actuators, B*, 2020, **308**, 127700, DOI: 10.1016/j.snb.2020.127700.

50 M. J. Szary and P. Radomski, Unveiling the Chemical Underpinnings behind the Enhanced Adsorption Interaction of NO_2 on MoS_2, $MoSe_2$, and $MoTe_2$ Transition Metal Dichalcogenides, *J. Phys. Chem. C*, 2023, **127**(43), 21374–21386, DOI: 10.1021/acs.jpcc.3c05101.

51 M. J. Szary, Toward high selectivity of sensor arrays: Enhanced adsorption interaction and selectivity of gas detection (N_2, O_2, NO, CO, CO_2, NO_2, SO_2, AlH_3, NH_3, and PH_3) on transition metal dichalcogenides (MoS_2, $MoSe_2$, and $MoTe_2$), *Acta Mater.*, 2024, **274**, 120016, DOI: 10.1016/j.actamat.2024.120016.

52 V. M. Bermudez, Computational study of the adsorption of NO_2 on monolayer MoS_2, *J. Phys. Chem. C*, 2020, **124**(28), 15275–15284, DOI: 10.1021/acs.jpcc.0c03786.

53 D. J. Late, Y.-K. Huang, B. Liu, J. Acharya, S. N. Shirodkar, J. Luo, A. Yan, D. Charles, U. V. Waghmare, V. P. Dravid and C. N. R. Rao, Sensing behavior of atomically thin-layered MoS_2 transistors, *ACS Nano*, 2013, **7**(6), 4879–4891, DOI: 10.1021/nn400026u, pMID: 23713986.

54 H. Wang, R. Xiong, H. Yang, Z. Qin, B. Sa, X. Wu, C. Xie and D. Zeng, Interlayer-expanded 2D VS_2 for fast response/recovery NO_2 detection at low-temperature, *Appl. Surf. Sci.*, 2022, **606**, 154894, DOI: 10.1016/j.apsusc.2022.154894.

55 X. Wang, Y. Zhang, H. Si, Q. Zhang, J. Wu, L. Gao, X. Wei, Y. Sun, Q. Liao, Z. Zhang, K. Ammarah, L. Gu, Z. Kang and Y. Zhang, Single-Atom Vacancy Defect to Trigger High-Efficiency Hydrogen Evolution of MoS_2, *J. Am. Chem. Soc.*, 2020, **142**(9), 4298–4308, DOI: 10.1021/jacs.9b12113.

56 L. Liu, M. Qing, Y. Wang and S. Chen, Defects in Graphene: Generation, Healing, and Their Effects on the Properties of Graphene: A Review, *J. Mater. Sci. Technol.*, 2015, **31**(6), 599–606, DOI: 10.1016/j.jmst.2014.11.019.

57 WHO global air quality guidelines, Particulate matter ($PM_{2.5}$ and PM_{10}), ozone, nitrogen dioxide, sulfur dioxide and carbon monoxide, *Executive Summary*, World Health Organization, Geneva, 2021.

58 World Health Organization, *World Health Statistics 2023: Monitoring Health for the SDGs, Sustainable Development Goals*, World Health Organization, Geneva, 2023.

59 M. Donarelli and L. Ottaviano, 2D Materials for Gas Sensing Applications: A Review on Graphene Oxide, MoS_2, WS_2 and Phosphorene, *Sensors*, 2018, **18**(11), 3638, DOI: 10.3390/s18113638.

60 P. Radomski and M. J. Szary, Transition metals vs. chalcogens: The impact on NO_x adsorption on MoS_2, $MoSe_2$ and WS_2 transition-metal dichalcogenides, *Acta Mater.*, 2024, **272**, 119949, DOI: 10.1016/j.actamat.2024.119949.

61 R. Kumar, N. Goel and M. Kumar, High performance NO_2 sensor using MoS_2 nanowires network, *Appl. Phys. Lett.*, 2018, **112**(5), 053502, DOI: 10.1063/1.5019296.

62 S. Kumar, G. Meng, P. Mishra, N. Tripathi and A. G. Bannov, A systematic review on 2D MoS_2 for nitrogen dioxide (NO_2) sensing at room temperature, *Mater. Today Commun.*, 2023, **34**, 105045, DOI: 10.1016/j.mtcomm.2022.105045.

63 T. Pham, G. Li, E. Bekyarova, M. E. Itkis and A. Mulchandani, MoS_2-Based Optoelectronic Gas Sensor with Sub-parts-per-billion Limit of NO_2 Gas Detection,

ACS Nano, 2019, **13**(3), 3196–3205, DOI: 10.1021/acsnano.8b08778.

64 M. Donarelli, S. Prezioso, F. Perrozzi, F. Bisti, M. Nardone, L. Giancaterini, C. Cantalini and L. Ottaviano, Response to NO_2 and other gases of resistive chemically exfoliated MoS_2-based gas sensors, *Sens. Actuators, B*, 2015, **207**, 602–613, DOI: 10.1016/j.snb.2014.10.099.

65 H. Li, Z. Yin, Q. He, H. Li, X. Huang, G. Lu, D. W. H. Fam, A. I. Y. Tok, Q. Zhang and H. Zhang, Fabrication of Single- and Multilayer MoS_2 Film-Based Field-Effect Transistors for Sensing NO at Room Temperature, *Small*, 2012, **8**(1), 63–67, DOI: 10.1002/smll.201101016.

66 Z. Wei, M. Liao, Y. Guo, J. Tang, Y. Cai, H. Chen, Q. Wang, Q. Jia, Y. Lu, Y. Zhao, J. Liu, Y. Chu, H. Yu, N. Li, J. Yuan, B. Huang, C. Shen, R. Yang, D. Shi and G. Zhang, Scratching lithography for wafer-scale MoS_2 monolayers, *2D Materials*, 2020, **7**(4), 045028, DOI: 10.1088/2053-1583/aba99f.

67 L. K. Tan, B. Liu, J. H. Teng, S. Guo, H. Y. Low and K. P. Loh, Atomic layer deposition of a MoS_2 film, *Nanoscale*, 2014, **6**(18), 10584–10588, DOI: 10.1039/C4NR02451F.

68 T. Jurca, M. J. Moody, A. Henning, J. D. Emery, B. Wang, J. M. Tan, T. L. Lohr, L. J. Lauhon and T. J. Marks, Low-Temperature Atomic Layer Deposition of MoS_2 Films, *Angew. Chem., Int. Ed.*, 2017, **56**(18), 4991–4995, DOI: 10.1002/anie.201611838.

69 M. Asadi, B. Kumar, A. Behranginia, B. A. Rosen, A. Baskin, N. Repnin, D. Pisasale, P. Phillips, W. Zhu, R. Haasch, R. F. Klie, P. Král, J. Abiade and A. Salehi-Khojin, Robust carbon dioxide reduction on molybdenum disulphide edges, *Nat. Commun.*, 2014, **5**(1), 4470, DOI: 10.1038/ncomms5470.

70 P. Abbasi, M. Asadi, C. Liu, S. Sharifi-Asl, B. Sayahpour, A. Behranginia, P. Zapol, R. Shahbazian-Yassar, L. A. Curtiss and A. Salehi-Khojin, Tailoring the Edge Structure of Molybdenum Disulfide toward Electrocatalytic Reduction of Carbon Dioxide, *ACS Nano*, 2017, **11**(1), 453–460, DOI: 10.1021/acsnano.6b06392.

71 P. D. Pedersen, T. Vegge, T. Bligaard and H. A. Hansen, Trends in CO_2 Reduction on Transition Metal Dichalcogenide Edges, *ACS Catal.*, 2023, **13**(4), 2341–2350, DOI: 10.1021/acscatal.2c04825.

72 B. Balan, M. M. Xavier and S. Mathew, MoS2-Based Nanocomposites for Photocatalytic Hydrogen Evolution and Carbon Dioxide Reduction, *ACS Omega*, 2023, **8**(29), 25649–25673, DOI: 10.1021/acsomega.3c02084.

73 J. Hu, L. Yu, J. Deng, Y. Wang, K. Cheng, C. Ma, Q. Zhang, W. Wen, S. Yu, Y. Pan, J. Yang, H. Ma, F. Qi, Y. Wang, Y. Zheng, M. Chen, R. Huang, S. Zhang, Z. Zhao, J. Mao, X. Meng, Q. Ji, G. Hou, X. Han, X. Bao, Y. Wang and D. Deng, Sulfur vacancy-rich MoS_2 as a catalyst for the hydrogenation of CO_2 to methanol, *Nat. Catal.*, 2021, **4**(3), 242–250, DOI: 10.1038/s41929-021-00584-3.

74 S. Zhou, W. Ma, U. Anjum, M. Kosari, S. Xi, S. M. Kozlov and H. C. Zeng, Strained few-layer MoS_2 with atomic copper and selectively exposed in-plane sulfur vacancies for CO_2 hydrogenation to methanol, *Nat. Commun.*, 2023, **14**(1), 5872, DOI: 10.1038/s41467-023-41362-y.

75 P. Giannozzi, S. Baroni, N. Bonini, M. Calandra, R. Car, C. Cavazzoni, D. Ceresoli, G. L. Chiarotti, M. Cococcioni, I. Dabo, A. D. Corso, S. de Gironcoli, S. Fabris, G. Fratesi, R. Gebauer, U. Gerstmann, C. Gougoussis, A. Kokalj, M. Lazzeri, L. Martin-Samos, N. Marzari, F. Mauri, R. Mazzarello, S. Paolini, A. Pasquarello, L. Paulatto, C. Sbraccia, S. Scandolo, G. Sclauzero, A. P. Seitsonen, A. Smogunov, P. Umari and R. M. Wentzcovitch, QUANTUM ESPRESSO: a modular and open-source software project for quantum simulations of materials, *J. Phys.: Condens. Matter*, 2009, **21**(39), 395502, DOI: 10.1088/0953-8984/21/39/395502.

76 P. Giannozzi, O. Andreussi, T. Brumme, O. Bunau, M. B. Nardelli, M. Calandra, R. Car, C. Cavazzoni, D. Ceresoli, M. Cococcioni, N. Colonna, I. Carnimeo, A. D. Corso, S. de Gironcoli, P. Delugas, R. A. D. Jr, A. Ferretti, A. Floris, G. Fratesi, G. Fugallo, R. Gebauer, U. Gerstmann, F. Giustino, T. Gorni, J. Jia, M. Kawamura, H.-Y. Ko, A. Kokalj, E. Küçükbenli, M. Lazzeri, M. Marsili, N. Marzari, F. Mauri, N. L. Nguyen, H.-V. Nguyen, A. O. de-la Roza, L. Paulatto, S. Poncé, D. Rocca, R. Sabatini, B. Santra, M. Schlipf, A. P. Seitsonen, A. Smogunov, I. Timrov, T. Thonhauser, P. Umari, N. Vast, X. Wu and S. Baroni, Advanced capabilities for materials modelling with QUANTUM ESPRESSO, *J. Phys.: Condens. Matter*, 2017, **29**(46), 465901.

77 P. Giannozzi, O. Baseggio, P. Bonfà, D. Brunato, R. Car, I. Carnimeo, C. Cavazzoni, S. de Gironcoli, P. Delugas, F. Ferrari Ruffino, A. Ferretti, N. Marzari, I. Timrov, A. Urru and S. Baroni, QUANTUM ESPRESSO toward the exascale, *J. Chem. Phys.*, 2020, **152**(15), 154105, DOI: 10.1063/5.0005082.

78 H. J. Monkhorst and J. D. Pack, Special points for brillouin-zone integrations, *Phys. Rev. B*, 1976, **13**, 5188–5192, DOI: 10.1103/PhysRevB.13.5188.

79 C. G. Broyden, The Convergence of a Class of Double-rank Minimization Algorithms 1. General Considerations, *IMA J. Appl. Math.*, 1970, **6**(1), 76–90, DOI: 10.1093/imamat/6.1.76.

80 R. Fletcher, A new approach to variable metric algorithms, *Comput. J.*, 1970, **13**(3), 317–322, DOI: 10.1093/comjnl/13.3.317.

81 D. Goldfarb, A family of variable-metric methods derived by variational means, *Math. Comput.*, 1970, **24**(109), 23–26, DOI: 10.1090/S0025-5718-1970-0258249-6.

82 D. F. Shanno, Conditioning of quasi-Newton methods for function minimization, *Math. Comput.*, 1970, **24**(111), 647–656, DOI: 10.1090/S0025-5718-1970-0274029-X.

83 P.-O. Löwdin, On the non-orthogonality problem connected with the use of atomic wave functions in the theory of molecules and crystals, *J. Chem. Phys.*, 1950, **18**(3), 365–375, DOI: 10.1063/1.1747632.

84 J. P. Perdew, K. Burke and M. Ernzerhof, Generalized gradient approximation made simple, *Phys. Rev. Lett.*, 1996, **77**, 3865–3868, DOI: 10.1103/PhysRevLett.77.3865.

85 J. P. Perdew, A. Ruzsinszky, G. I. Csonka, O. A. Vydrov, G. E. Scuseria, L. A. Constantin, X. Zhou and K. Burke, Restoring the density-gradient expansion for exchange in solids and surfaces, *Phys. Rev. Lett.*, 2008, **100**, 136406, DOI: 10.1103/PhysRevLett.100.136406.

86 X. Lin, W. Li, Y. Dong, C. Wang, Q. Chen and H. Zhang, Two-dimensional metallic MoS_2: A DFT study, *Comput. Mater. Sci.*, 2016, **124**, 49–53, DOI: 10.1016/j.commatsci.2016.07.020.

87 S. A. Yamusa, A. Shaari, N. A. M. Alsaif, I. M. Alsalamah, I. Isah and N. Rekik, Elucidating the Structural, Electronic, Elastic, and Optical Properties of Bulk and Monolayer MoS_2 Transition-Metal Dichalcogenides: A DFT Approach, *ACS Omega*, 2022, **7**(49), 45719–45731, DOI: 10.1021/acsomega.2c07030.

88 H.-P. Komsa and A. V. Krasheninnikov, Native defects in bulk and monolayer MoS_2 from first principles, *Phys. Rev. B:Condens. Matter Mater. Phys.*, 2015, **91**(12), 125304, DOI: 10.1103/PhysRevB.91.125304.

89 L. Debbichi, O. Eriksson and S. Lebègue, Electronic structure of two-dimensional transition metal dichalcogenide bilayers from ab initio theory, *Phys. Rev. B*, 2014, **89**(20), 205311, DOI: 10.1103/PhysRevB.89.205311.

90 J. Cha, D. Sung, K.-A. Min and S. Hong, Van der Waals Density Functional Theory Study of Molecular Adsorbates on MoX_2(X = S, Se or Te), *J. Korean Phys. Soc.*, 2018, **73**(1), 100–104, DOI: 10.3938/jkps.73.100.

91 S. Grimme, Semiempirical GGA-type density functional constructed with a long-range dispersion correction, *J. Comput. Chem.*, 2006, **27**(15), 1787–1799, DOI: 10.1002/jcc.20495.

92 S. Grimme, J. Antony, S. Ehrlich and H. Krieg, A consistent and accurate ab initio parametrization of density functional dispersion correction (DFT-D) for the 94 elements H-Pu, *J. Chem. Phys.*, 2010, **132**(15), 154104, DOI: 10.1063/1.3382344.

93 M. J. Szary, A dsorption of ethylene oxide on doped monolayers of MoS_2: A DFT study, *Mater. Sci. Eng., B*, 2021, **265**, 115009, DOI: 10.1016/j.mseb.2020.115009.

94 M. J. Szary, D. M. Florjan and J. A. Bąbelek, Selective Detection of Carbon Monoxide on P-Block Doped Monolayers of $MoTe_2$, *ACS Sens.*, 2022, **7**(1), 272–285, DOI: 10.1021/acssensors.1c02246.

95 D. M. Florjan and M. J. Szary, Enhancing surface activity in $MoTe_2$ monolayers through p-block doping: A comprehensive DFT investigation, *Acta Mater.*, 2024, **272**, 119951, DOI: 10.1016/j.actamat.2024.119951.

96 M. J. Szary, J. A. Bąbelek and D. M. Florjan, Adsorption and dissociation of NO_2 on MoS_2 doped with p-block elements, *Surf. Sci.*, 2021, **712**, 121893, DOI: 10.1016/j.susc.2021.121893.

97 J. Klimeš, D. R. Bowler and A. Michaelides, Chemical accuracy for the van der Waals density functional, *J. Phys.: Condens. Matter*, 2009, **22**(2), 022201, DOI: 10.1088/0953-8984/22/2/022201.

98 J. Klimeš, D. R. Bowler and A. Michaelides, Van der Waals density functionals applied to solids, *Phys. Rev. B*, 2011, **83**(19), 195131, DOI: 10.1103/PhysRevB.83.195131.

99 I. Hamada, van der Waals density functional made accurate, *Phys. Rev. B*, 2014, **89**(12), 121103, DOI: 10.1103/PhysRevB.89.121103.

100 K. D. Bronsema, J. L. De Boer and F. Jellinek, On the structure of molybdenum diselenide and disulfide, *Z. Anorg. Allg. Chem.*, 1986, **540**(9–10), 15–17, DOI: 10.1002/zaac.19865400904.

101 P. Joensen, R. F. Frindt and S. R. Morrison, Single-layer MoS_2, *Mater. Res. Bull.*, 1986, **21**(4), 457–461, DOI: 10.1016/0025-5408(86)90011-5.

102 A. Kokalj, XCrySDen–a new program for displaying crystalline structures and electron densities, *J. Mol. Graphics Modell.*, 1999, **17**(3), 176–179, DOI: 10.1016/S1093-3263(99)00028-5.

103 J. Sanders, *Veusz: Scientific Plotting Package, Astrophysics Source Code Library (2023) ascl:2307.017ADS Bibcode: 2023ascl.soft07017S*, 2023.

104 P. Man, S. Jiang, K. H. Leung, K. H. Lai, Z. Guang, H. Chen, L. Huang, T. Chen, S. Gao, Y.-K. Peng, C.-S. Lee, Q. Deng, J. Zhao and T. H. Ly, Salt-induced high-density vacancy-rich 2D MoS_2 for efficient hydrogen evolution, *Adv. Mater.*, 2024, **36**(17), 2304808, DOI: 10.1002/adma.202304808.

105 Y. Linghu, D. Lu and C. Wu, Cooxidation over defective and nonmetal doped MoS_2 monolayers, *J. Phys.: Condens. Matter*, 2021, **33**(16), 165002, DOI: 10.1088/1361-648X/abeff9.

106 G. Brehm, M. Reiher and S. Schneider, Estimation of the Vibrational Contribution to the Entropy Change Associated with the Low- to High-Spin Transition in $Fe(phen)_2(NCS)_2$ Complexes: Results Obtained by IR and Raman Spectroscopy and DFT Calculations, *J. Phys. Chem. A*, 2002, **106**(50), 12024–12034, DOI: 10.1021/jp026586o.

107 A. J. Meier, A. Garg, B. Sutter, J. N. Kuhn and V. R. Bhethanabotla, MoS_2 Nanoflowers as a Gateway for Solar-Driven CO_2 Photoreduction, *ACS Sustain. Chem. Eng.*, 2019, **7**(1), 265–275, DOI: 10.1021/acssuschemeng.8b03168.

108 S. Aftab, M. Zahir Iqbal, S. Hussain, H. H. Hegazy, F. Kabir, S. Hassan Abbas Jaffery and G. Koyyada, New developments in gas sensing using various two-dimensional architectural designs, *Chem. Eng. J.*, 2023, **469**, 144039, DOI: 10.1016/j.cej.2023.144039.

109 M. J. Szary, Al doped MoS_2 for adsorption-based water collection, *Appl. Surf. Sci.*, 2020, **529**, 147083, DOI: 10.1016/j.apsusc.2020.147083.

110 N. Moses Badlyan, N. Pettinger, N. Enderlein, R. Gillen, X. Chen, W. Zhang, K. C. Knirsch, A. Hirsch and J. Maultzsch, Oxidation and phase transition in covalently functionalized MoS_2, *Phys. Rev. B*, 2022, **106**, 104103, DOI: 10.1103/PhysRevB.106.104103.

111 S. J. Kim, J. Y. Park, S. Yoo, P. Umadevi, H. Lee, J. Cho, K. Kang and S. C. Jun, Carrier transport properties of MoS_2 asymmetric gas sensor under charge transfer-based

barrier modulation, *Nanoscale Res. Lett.*, 2018, **13**(1), 265, DOI: **10.1186/s11671-018-2652-9**.

112 Y. Shi, W. Zhang, J. Tan, T. Yan, Y. Jia, Z. Wang, Y. Tang and Q. Gao, Intercalation-driven defect-engineering of MoS_2 for catalytic transfer hydrogenation, *Adv. Mater. Interfaces*, 2022, **9**(16), 2200505, DOI: **10.1002/admi.202200505**.

113 T. Sekine, C. Julien, I. Samaras, M. Jouanne and M. Balkanski, Vibrational modifications on lithium intercalation in MoS_2, *Mater. Sci. Eng., B*, 1989, **3**(1), 153–158, DOI: **10.1016/0921-5107(89)90195-5**.

114 J. C. Chacón-Torres, L. Wirtz and T. Pichler, Manifestation of Charged and Strained Graphene Layers in the Raman Response of Graphite Intercalation Compounds, *ACS Nano*, 2013, **7**(10), 9249–9259, DOI: **10.1021/nn403885k**.

115 Y. Wu, J. Wang, Y. Li, J. Zhou, B. Y. Wang, A. Yang, L.-W. Wang, H. Y. Hwang and Y. Cui, Observation of an intermediate state during lithium intercalation of twisted bilayer MoS_2, *Nat. Commun.*, 2022, **13**(1), 3008, DOI: **10.1038/s41467-022-30516-z**.

116 Y. Sun, S. Yin, R. Peng, J. Liang, X. Cong, Y. Li, C. Li, B. Wang, M.-L. Lin, P.-H. Tan, C. Wan and K. Liu, Abnormal Out-of-Plane Vibrational Raman Mode in Electrochemically Intercalated Multilayer MoS_2, *Nano Lett.*, 2023, **23**(11), 5342–5349, DOI: **10.1021/acs.nanolett.3c01543**.

117 L. Huang, Y. Li, Z. Wei and J. Li, Strain induced piezoelectric effect in black phosphorus and MoS_2 van der Waals heterostructure, *Sci. Rep.*, 2015, **5**(1), 16448, DOI: **10.1038/srep16448**.

118 Z. Li, W. Zhao, Q. Zhang, Q. Zhou, J. Liang, Z. Cai, M. Zhang, C. Yang, S. Sun, Y. Luo, D. Zheng, F. Gong, Y. Yao, Y. Lin and X. Sun, Pie zoelectric MoS_2 with expanded interlayers: a flexible anode for a "zero" interfacial quasi-solid-state ammonium-ion asymmetric supercapacitor, *J. Mater. Chem. A*, 2024, **12**(36), 24084–24090, DOI: **10.1039/D4TA04691A**.

119 Z. Wang, H. Zhong, Z. Zhu, H. Zhang, Y. Qiu and D. Yin, Few-layer MoS_2 nanosheets modified by PEG for enhanced piezoelectric catalysis degradation of carbamazepine, *Chem. Eng. J.*, 2024, **497**, 154631, DOI: **10.1016/j.cej.2024.154631**.